ČESKÉ VYSOKÉ UČENÍ TECHNICKÉ V PRAZE

TEZE K DISERTAČNÍ PRÁCI

České vysoké učení technické v Praze
Fakulta jaderná a fyzikálně inženýrská
Katedra fyzikální elektroniky

Ing. Pavel Kwiecien

Analýza a modelování subvlnových struktur pomocí Fourierovských modálních metod

Doktorský studijní program: Aplikace přírodních věd
Studijní obor: Fyzikální inženýrství

Teze disertace k získání akademického
titulu „doktor" ve zkratce „Ph.D."

Praha, březen, 2015

Disertační práce byla vypracována v prezenční/kombinované formě doktorského studia na Katedře fyzikální elektroniky Fakulty jaderné a fyzikálně inženýrské ČVUT v Praze.

Uchazeč:	Ing. Pavel Kwiecien Katedra fyzikální elektroniky Fakulta jaderná a fyzikálně inženýrská ČVUT v Praze Břehova 7, 11519 Praha 1
Školitel:	doc. Ing. Ivan Richter, Dr. Katedra fyzikální elektroniky Fakulta jaderná a fyzikálně inženýrská ČVUT v Praze Břehova 7, 11519 Praha 1
Školitel specialista:	prof. Ing. Jiří Čtyroký, DrSc. Ústav fotoniky a elektroniky AV ČR, v. v. i. Chaberská 57, 18251 Praha 8 — Kobylisy
Oponenti:	doc. Mgr. Kamil Postava, Dr. Institut fyziky VŠB — Technická univerzita Ostrava 17. listopadu 15, 708 33 Ostrava — Poruba RNDr. Roman Antoš, Ph.D. Fyzikální ústav MFF UK, Ke Karlovu 5, 121 16 Praha 2

Teze byly rozeslány dne: ....

Obhajoba disertace se koná dne .... v .... hod. před komisí pro obhajobu disertační práce ve studijním oboru fyzikální inženýrství v zasedací místnosti č. L244, Katedry fyzikální elektroniky Fakulty jaderné a fyzikálně inženýrské ČVUT v Praze, v areálu MFF UK, V Holešovičkách 2, Praha 8.

S disertací je možno se seznámit na děkanátě Fakulty jaderné a fyzikálně inženýrské ČVUT v Praze, na oddělení pro vědeckou a výzkumnou činnost, Břehová 7, Praha 1.

doc. Ing. Ladislav Pína, DrSc.
předseda komise pro obhajobu disertační práce
ve studijním oboru
Fyzikální inženýrství Fakulta jaderná a
fyzikálně inženýrská ČVUT, Břehová 7, Praha 1

Contents

Introduction

Currently, as photonic and plasmonic structures and elements with sub-wavelength feature sizes are becoming very attractive components for integrated optics and photonics devices in general, among other important experimental and technological aspects, new theoretical exploitations and modelling activities are of high interest in connection towards their direct application to realistic 3D geometries and problems to be solved and optimised. Clearly, such demands require very efficient and reliable computational methods based on various principles and theoretical considerations; these methods are often based either on the time-domain approach (mostly represented with the finite-difference time-domain – FDTD – method nowadays) or on the frequency-domain approaches, with both advantages and disadvantages in these main categories. Among the frequency-domain methods available nowadays, the "clever" physically oriented modal methods have proven themselves as very efficient and reliable tools for modelling such (sub) wavelength-sized photonics structures, including plasmonic devices, which are of general interest in current scientific activities. Although these modal techniques have been originally developed as mode expansion tools for guided-wave devices, and have gained a tremendous success in standard integrated-optical modelling tasks, quite recently, they have been inspired with the earlier-developed Rigorous coupled wave analysis (RCWA) method; also called as Fourier modal methods (FMM); based on Fourier expansions [1].

This, in fact, has led to the improvement in numerical stability and algorithm performance. Such methods have been named with the attribute aperiodic in connection to the terminology of the periodic method, hence, the terms "aperiodic" Rigorous coupled wave analysis (aRCWA), or perhaps more generally, aperiodic Fourier modal method (aFMM). Within this text, as is also the tradition in our research, we will opt for the former term aRCWA. To avoid confusion, by the term "3D aRCWA" we mean the aperiodic version of 2D-periodic grating algorithm RCWA. Therefore, by the term "2D aRCWA" we mean the aperiodic version of 1D-periodic grating algorithm RCWA.

Goals of the thesis

- Numerical implementation of the 2D-periodic RCWA, research and implementation of related special features (various Fourier factorization schemes, ASR, NVM, symmetries, . . .).
- Implementation of the 3D aRCWA method with relevant special features, based on 2D-periodic RCWA.
- Research and implementation of other (a)RCWA-like algorithms (1D full-anisotropic RCWA, 2D magneto-optic aRCWA, . . .), according to actual requirement.
- Thorough testing and optimization of developed methods.

- Application of the methods to investigated photonic and plasmonic sub-wavelength structures. Mainly, as represented in this thesis (localized surface plasmons based sensors, one-way plasmonic waveguides, hybrid plasmonic waveguides, high-Q photonic crystal nanocavities, and segmented sub-wavelength grating waveguides).

The secondary goals of this work include the development of other methods (e.g. nonlinear 2D aRCWA method, nonlinear Complex Jacobi method, ...) and application of (a)RCWA methods to other areas of interest (e.g. metamaterials, surface plasmon resonance sensors, sub-wavelength metallic apertures, ...). We note that the 2D aRCWA method has been studied and implemented in the master's thesis [2].

1 Numerical methods in photonics

Fabricating prototypes of optical components especially in the fields of photonics and plasmonics is time consuming and very expensive. It is therefore no longer feasible to choose the best design by fabricating a large set of possible alternatives and then evaluating them experimentally. This means several cycles of fabrication, testing, characterization, re-design, and finally, fabrication again. The only possible approach therefore is to resort to computer models that simulate the optical behaviour of the different designs in an accurate and speedy manner. Photonics is especially suitable for computation because we can predict the optical properties of the proposed structure by simply solving Maxwell's equations on a computer. This is obviously faster and cheaper than fabrication. We can simulate the structure first and redesign numerically until we get the ideal, optimised structure before doing any fabrication.

From the physical point of view, numerical methods in photonics can be divided according to type of solution to two major tasks groups:

1. Waveguide mode calculation, i.e. the computation of propagation constants in waveguides and mode shapes. Computer programs are often referred to as "mode solvers".

2. Evolution of the optical field/mode in the structure. The aim is to calculate the field distribution and evolution of optical radiation in longitudinally inhomogeneous elements.

Some of the numerical methods can simultaneously be used as mode solvers and as wave propagators: e.g. the finite-difference method, the finite element method, or eigenmode/modal expansion methods.

There exist a variety of optical models, there is no optimal numerical method which can effectively solve all the investigated structures. Let us mention here only the most important methods.

- Finite element method ([3])

- Finite-difference method ([4])

- Finite-difference time-domain method ([5])

- Beam propagation method ([4])
- Method of lines ([6])
- Boundary element method ([7])
- Eigenmode expansion method ([8])

Classification of (aperiodic) rigorous coupled wave analysis

This work deals with the (aperiodic) rigorous coupled wave analysis, in a wider sense also frequently called FMM (Fourier modal method). In contrast with eigenmode expansion method, where the field expansion is determined for each homogeneous medium by finding all the contributing modes and then matched at the boundaries, in the case of the (a)RCWA method, the field expansion is obtain from the Fourier representation of the permittivity/permeability profile. From this point of view, the (a)RCWA method can be addressed as the eigenmode method by Fourier expansion.

Finally, high quality "black box" software is widely available, including free, open source programs. Numerous software packages are available for problems and can easily be found in the usual catalogues. Usually commercial codes are usually tailored to efficient solutions of routine design problems and fail to accurately simulate high-end problems found in cutting-edge research. Therefore, research in computational photonics is still ongoing.

2 aRCWA algorithm

This chapter is devoted to the theoretical derivation of the 3D aperiodic Rigorous coupled wave analysis (aRCWA) method. This chapter contains the description of all important extensions of the 3D aRCWA method which we have employed.

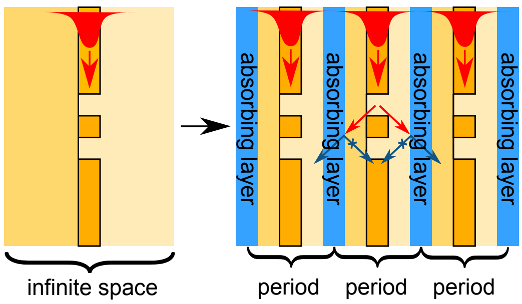

Figure 1 Schematic picture of 2D aRCWA principles: 1D artificial periodization.

Rigorous coupled wave analysis (also called the Fourier modal method) [9] is an efficient tool for the numerical analysis of periodical structures. The RCWA method is based on the expansion of the electromagnetic field and material properties (permittivity / permeability) into (Floquet) - Fourier series. To solve the electromagnetic modes, given typically, by the wave vector of the incident plane wave of the electric field, in periodic medium, the Maxwell's equations (in partial differential form) are expanded by the Floquet-Fourier functions and turned into infinitely large algebra equations. Next, with the cutting off of higher order Fourier functions, depending on the accuracy and convergence speed one needs, the infinitely large algebraic equations become finite and thus solvable by computers.

To extend the use of the standard periodic RCWA method, absorbing layers can be introduced such that the model can mimic a non-periodic structure [10, 1]. Proper absorbing layers numerically isolate the materials and propagating modes within a unit period from its neighbouring periods and will dampen all energy scattered from guided modes in the unit period. For example, let us have a waveguide structure that extends to infinity in the vertical dimension, as depicted in Fig. 1 (left). To model it using the RCWA method, we have to force the layer to a finite and repetitive computational domain by reducing the infinite space that extends outside the waveguide structure, see Fig. 1 (right). In the last couple of years, we have already demonstrated and effectively applied this method in 2D aRCWA case [11].

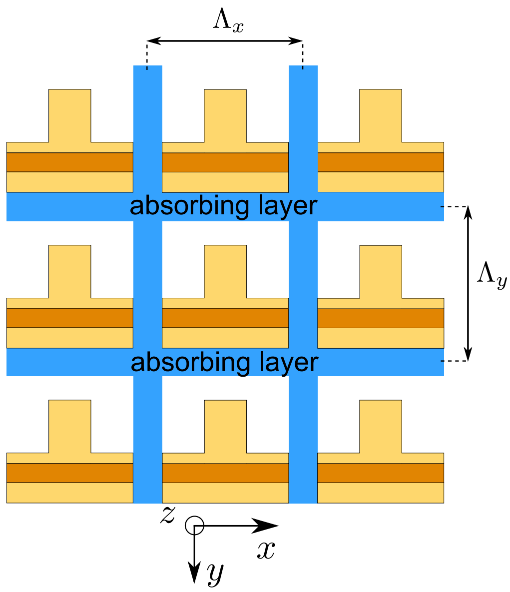

Figure 2 Schematic picture of 3D aRCWA principles: 2D artificial periodization of the 3D structure cross section.

The waveguiding problem of the multilayer structure (see Fig. 3) is solved in a sequence of steps. First, the coupled-wave equations are constructed and solved for the electromagnetic fields in each layer (see Fig. 4). Secondly, the electromagnetic boundary conditions (continuity of the tangential electric- and magnetic-field components) are applied between the input region and the first layer, then between the first and the second layer, and so forth, and finally between the last grating and the output region. Third, the resulting array of boundary condition equations is solved for the reflected and transmitted field amplitudes, and diffraction efficiencies are determined. These steps are discussed in the sections below.

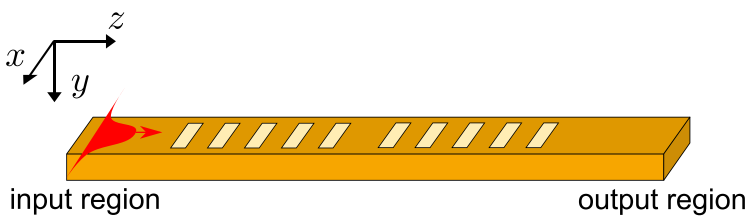

Figure 3 Geometry of a 3D photonic waveguide structure.

The extension into real 3D structure calculations causes a very strong increase of the number of Fourier terms. This increase is not only due to two independent transverse dimensions in play, but also due to generally hybrid character of eigenmodes of 3D structures.
Clearly, the first step for the 3D aRCWA represents the development of an efficient 2D periodic RCWA tool, as discussed further in section 2.3, optimally with all efficient up-to-date techniques already included as shown Fig. 5, i.e. mainly the critical convergence issues, via the application of proper Fourier factorization rules described in section 2.2. As the next step, in order to proceed towards the 2D mode solver, following the same idea as in 1D case, again, the isolating boundary conditions applied on the boundaries of a 2D period have to be utilized (see Fig. 2) where the schematic artificial periodization in 2D

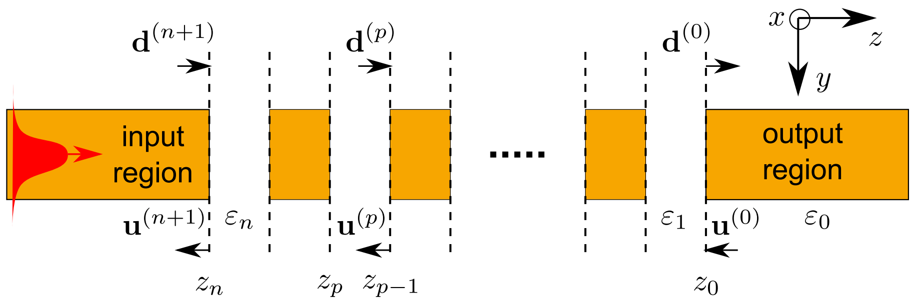

Figure 4 Side view of the photonic waveguide structure. The structure is composed of n sub-regions, the thickness of layer (p) is given by $(z_{p-1} - z_p)$. The layers (0) and $(n+1)$ describe the output and input region, respectively. The modes $\mathbf{u}^{(p)}$ and $\mathbf{d}^{(p)}$ describe the upwards and downwards propagating modes in layer (p), respectively.

is illustrated. The most effective absorbing boundary layers applicable in this case are the Perfectly matched layer (PML) type boundaries described in section 2.4. Additionally, if the typical dimensions of the structural sections or their permittivities are of huge mutual difference, another technique, called the Adaptive spatial resolution (ASR) can be very helpful; the ASR technique is discussed in section 2.5. Next, moving from 2D to 3D case, the number of expansion terms in the Fourier modal methods rapidly increases; the total number of expansion terms is namely twice the product of the particular expansion numbers in each of the two transverse directions. To reduce this problem at least partially, structural symmetries of the simulated objects can be fully utilized. As the final step, as the propagation extension of the 2D mode solver, advanced schemes of numerically-stable scattering matrices is included.

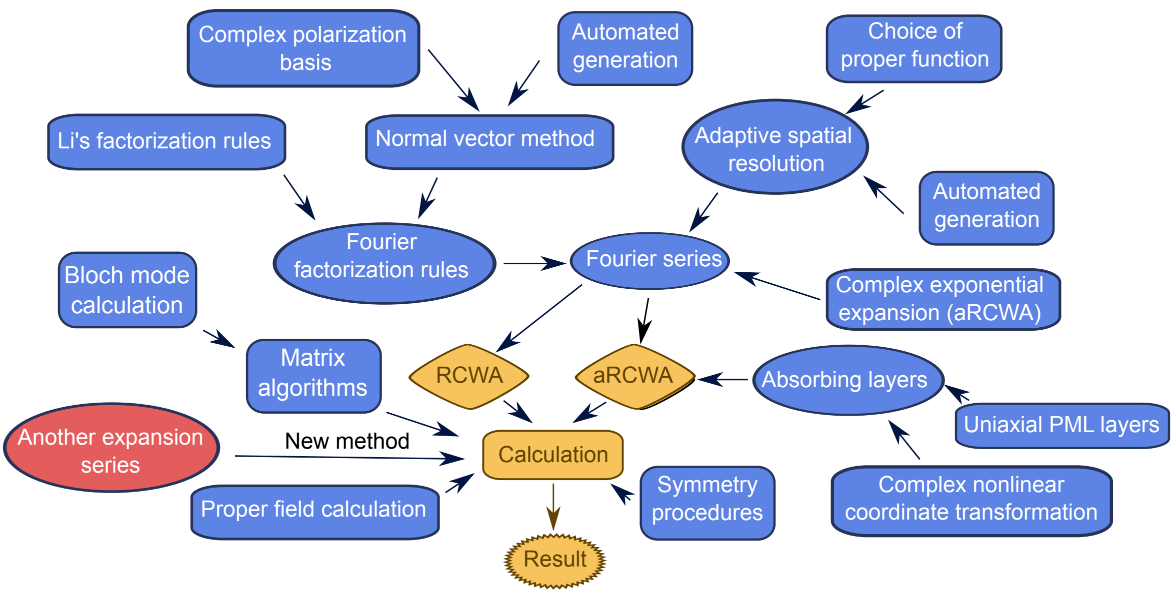

Figure 5 Schematic diagram of our (a)RCWA method development; various modifications to several critical parts within the algorithm have appeared, showing either partial or even strong improvement in terms of performance / time efficiency and capabilities. Points indicated in blue colour are of direct concern within the scope of this thesis.

We assume a time dependence of all fields of the form $\exp(-\mathrm{i}\omega t)$. An input mode with wavelength λ illuminates the structure under normal incidence. For simplicity, we limit our analysis to materials with diagonal $\overleftrightarrow{\varepsilon}$ and $\overleftrightarrow{\mu}$. Definitely, we will analyse here only the eigenmode problem in the longitudinally uniform sections of the photonic structure to be modelled. Each such section is considered as a multilayer structure with stepwise transverse permittivity profile. Fig. 4 gives a side view of the photonic waveguide structure shown in 3. The structure is composed of n layers (after multilayer approximation), each of which is non-varying in the z direction, with the thickness of a particular region (p) given by $z_{p-1} - z_p$. The incident mode is sent typically from the input region $(n+1)$ and the transmitted mode propagates in the output (region (0)). The modes $\mathbf{u}^{(p)}$ and $\mathbf{d}^{(p)}$ describe the upwards and downwards propagating modes in layer (p).

To start the analysis, let us write the Maxwell's curl equations in covariant form:

$$\varepsilon_{\rho\sigma\tau}\partial_\sigma E_\tau = \mathrm{i}k_0\sqrt{g_T}\mu^{\rho\sigma}H_\sigma, \tag{1}$$

$$\varepsilon_{\rho\sigma\tau}\partial_\sigma H_\tau = -\mathrm{i}k_0\sqrt{g_T}\varepsilon^{\rho\sigma}E_\sigma, \tag{2}$$

where $\varepsilon_{\rho\sigma\tau}$ is the Levi-Civita tensor. Here, we use the Einstein summation rule over repeated indices and note that a separate equation is represented for each of the three values of ρ. These equations are formulated in a covariant form to apply simple coordinate transformations in two dimensions for the application for the adaptive spatial resolution technique and the perfectly matched layer. Since we consider only the rectangular Cartesian coordinate system $(\sigma = x, y, z)$ and a uniaxial medium in the following analysis, due to simplicity reason, the covariant metric tensor g_T is equal to one (despite this simplification, our software tool RCWA-2D supports a non-rectangular Cartesian coordinate). Writing out the summations and separate equations explicitly yields the following set of equations:

$$\partial_y H_z - \partial_z H_y = -\mathrm{i}k_0\varepsilon_{11}E_x, \tag{3}$$

$$\partial_z H_x - \partial_x H_z = -\mathrm{i}k_0\varepsilon_{22}E_y, \tag{4}$$

$$\partial_x H_y - \partial_y H_x = -\mathrm{i}k_0\varepsilon_{33}E_z, \tag{5}$$

$$\partial_y E_z - \partial_z E_y = \mathrm{i}k_0\mu_{11}H_x, \tag{6}$$

$$\partial_z E_x - \partial_x E_z = \mathrm{i}k_0\mu_{22}H_y, \tag{7}$$

$$\partial_x E_y - \partial_y E_x = \mathrm{i}k_0\mu_{33}H_z. \tag{8}$$

In brief, the aRCWA method involves finding solutions of Eqs. (3)–(8) in each region (i) and connecting these solutions by the boundary conditions at the region interfaces.

2.1 Expansion of electromagnetic field

Until now, we only formulate Maxwell's equations in the frequency domain. To solve Maxwell's equations rigorously, the electromagnetic fields can be decomposed into a basis set of local eigenmodes. Compared to the true modal method [12] which tries to find the exact solution of the field inside the grating, the RCWA method uses the (Floquet-)Fourier series expansion of the material profile to obtain the mode expansion of the field.

The advantage of the Fourier series is that it is easy to implement, moreover, the RCWA method is applicable to many types of periodic structure compared to true modal method.

As we have noted, the electromagnetic field may be expanded into (Floquet-)Fourier series (the field in the doubly periodic medium is a pseudoperiodic function)

$$E_\sigma(x, y, z) = \sum_{m,n} E_{\sigma,mn}(z)\, \mathrm{e}^{\mathrm{i}(\alpha_m x + \beta_n y)}, \tag{9}$$

$$H_\sigma(x, y, z) = \sum_{m,n} H_{\sigma,mn}(z)\, \mathrm{e}^{\mathrm{i}(\alpha_m x + \beta_n y)}, \tag{10}$$

where $\sigma = x, y, z$, $\alpha_m = 2\pi m/\Lambda_x$ and $\beta_n = 2\pi n/\Lambda_y$, where Λ_x and Λ_y are periods in the x direction and in the y direction respectively (see Fig. 2); m and n are integers. Next, Eqs. (9)–(10) will be inserted into Maxwell's equations (3)–(8), but due to numerical truncation of the Fourier series, Maxwell's equations must be correctly converted into linear algebraic systems in the discrete Fourier space, as shown in the next section.

Let us now study truncation of the Fourier series. Let m and n are integers such that $-N_x \le m \le N_x$ and $-N_y \le n \le N_y$, where the integers N_x and N_y describe the truncation order in the x direction and the y direction, respectively (in practice, they are often equal, i.e. $N_x = N_y$). A total $n_{xy} = (2N_x + 1)(2N_y + 1)$ orders have to be included in the analysis.

2.2 Factorization rules

When the (a)RCWA method is implemented in practice, it is clear that the Fourier expansions must be truncated. As a result, quantities, that in an infinite Fourier expansion are equivalent, may not be so in practice. Since the birth of the RCWA method, there had been an issue with a convergence for planar diffraction (1D period) in the case of TM polarization. The TM polarization convergence was slow and poor while the convergence for the TE polarization was rapid and fully comparable with other methods. Important changes in the algorithm for the TM case were performed in articles [13, 14], they, indeed, brought a dramatic improvement of the convergence in the case of TM polarization, but they were made without any mathematical explanation. In fact, mathematical explanation of the improved TM polarization convergence brought Lifeng Li in [15]. Later Li [16] applied factorization rules to the 2D periodic structures, too.

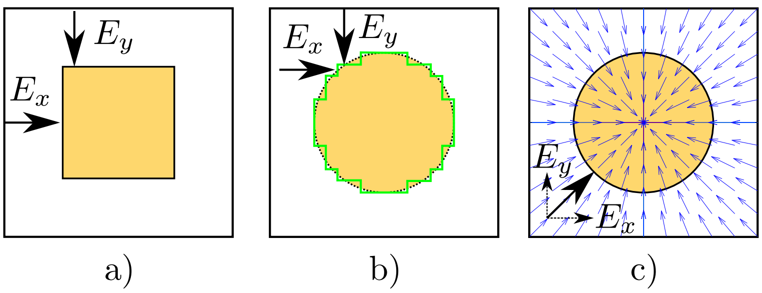

Figure 6 Example of various possibilities of Fourier factorization techniques: Li's factorization: a) rectangular shape, b) non-rectangular shape; Normal vector method: c) non-rectangular shape.

Firstly, we will review Li's factorization rules for 2D gratings. This formulation is suitable for gratings composed of rectangular shapes as shown in Fig. 6a), in case of non-rectangular shapes (see Fig. 6b), as an illustrative example), this technique brings inaccuracy due to zigzag discretization.

Later paper [17] introduce an idea of the Normal vector method (also called in another literature as the Fast Fourier factorization). This technique is based on the decomposition of the electric field displacement vector into a normal and tangential component at each boundary point (see Fig. 6c)). Therefore, the Li's factorization rules are fulfilled at any point on the material interface, hence there is no need to use the zigzag discretization. Let us study these techniques in a more detail.

2.2.1 Li's factorization rules for 2D gratings

For the 1D case, paper [15] showed that the slow convergence was connected with the erroneous use of Laurent's rule to factor the Fourier coefficient of a product of functions with complementary jumps (discontinuities). Additionally, paper [15] brought rules for the so-called proper Fourier factorization of different types of products, the rules are as follows:

- A product of type 1 (two piecewise-smooth, bounded, periodic functions that have no concurrent jump discontinuities) can be Fourier factorized by Laurent's rule.
- A product of type 2 (two piecewise-smooth, bounded, periodic functions that have only pairwise complementary jump discontinuities) cannot be Fourier factorized by Laurent's rule, but in most cases it can be Fourier factorized by the inverse rule.
- A product of type 3 (two piecewise-smooth, bounded, periodic functions that have concurrent but not complementary jump discontinuities) can be Fourier factorized by neither Laurent's rule nor the inverse rule.

The Fourier factorization based on paper [15] is valid only for rectangular objects. In order to factorize an arbitrary object using this technique, zigzag discretization of the object must be used. Mesh discretization has a great influence on the accuracy of results especially in the case of metallic structures.

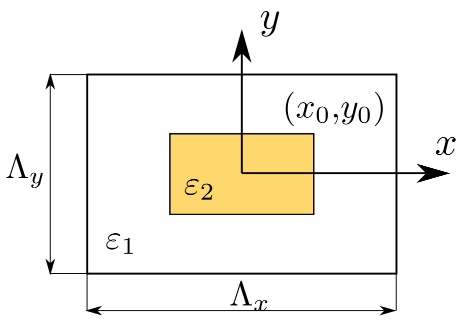

Figure 7 A unit cell of the grating with periods Λ_x and Λ_y.

Further, as we need to carry out the Fourier analysis of equations (3)–(8), we start with equations (3)–(5). Fig. 7 shows a unit cell of a 2D grating with periods Λ_x and Λ_y. The modal fields in this case are piecewise continuous, piecewise smooth, and pseudoperiodic functions of x and y. The electric and magnetic field components transverse to the z-axis are in general singular at the edges of the grating profile, but they should be absolutely square-integrable because the electromagnetic energy enclosed in any finite volume must be finite.

Initially, we begin with equation (5). This equation can be directly factorized by Laurent's rule in the x and y directions, since E_z is continuous function in the z direction, thus the product $\varepsilon_{33}E_z$ is a product of type 1, we obtain

$$(\varepsilon_{33}E_z)_{mn} = \sum_{jl} [\![\varepsilon_{33}]\!]_{mn,jl}\, E_{zjl}, \tag{11}$$

where the first integer subscript before and after the comma in both cases are associated with the Fourier coefficients in the x-direction and the second subscript in the y-direction respectively. An element $[\![\varepsilon]\!]$ is a matrix generated by the double Fourier coefficients of $\varepsilon(x,y)$ such that $[\![\varepsilon]\!]_{mn,jl} = \varepsilon_{m-j,n-l}$.

Next, the Fourier factorization of equation (3) is slightly more complicated. The product $\varepsilon_{11}E_x$ is a product of type 1 across the vertical y boundaries and a product of type 2 across the horizontal x boundaries. The Fourier analysis can be performed along the two directions separately, and along each direction the product is of only one type. Firstly, we have to apply the inverse rule in the x direction

$$(\varepsilon_{11}E_x)_m = \sum_j \left\lceil \frac{1}{\varepsilon_{11}} \right\rceil^{-1} E_{xj}(y), \tag{12}$$

where $\lceil f \rceil$ is the matrix generated by the Fourier coefficients of function $f(x,y)$ with respect to variable x. Secondly, we have to apply the Laurent's rule in the y direction.

$$(\varepsilon_{11}E_x)_{mn} = \sum_{jl} \lfloor\lceil\varepsilon_{11}\rceil\rfloor_{mn,jl} E_{xjl}, \tag{13}$$

where we have introduced the symbol $\lfloor\lceil\varepsilon_{11}\rceil\rfloor_{mn,jl} = \left\lfloor \lceil 1/\varepsilon_{11}\rceil^{-1}_{nl} \right\rfloor_{mj}$. A matrix $\lfloor f \rfloor$ is generated by the Fourier coefficients of function $f(x,y)$ with respect to variable y.

The Fourier factorization of equation (4) is similar to previous case; however, we must apply the inverse rule in the y direction and Laurent's rule in the x direction, thus

$$(\varepsilon_{22}E_y)_{mn} = \sum_{jl} \lceil\lfloor\varepsilon_{22}\rfloor\rceil_{mn,jl} E_{yjl}, \tag{14}$$

where $\lceil\lfloor\varepsilon_{22}\rfloor\rceil_{mn,jl} = \left\lceil \lfloor 1/\varepsilon_{22}\rfloor^{-1}_{nl} \right\rceil_{mj}$.

To sum up, we rewrite equations (11,13, and 14) into a more compact form. The relation between the electric displacement field and the electric field in the Fourier domain is given by

$$\begin{pmatrix} D_{xmn} \\ D_{ymn} \\ D_{zmn} \end{pmatrix} = \begin{pmatrix} Q_{\varepsilon,11} & Q_{\varepsilon,12} & Q_{\varepsilon,13} \\ Q_{\varepsilon,21} & Q_{\varepsilon,22} & Q_{\varepsilon,23} \\ Q_{\varepsilon,31} & Q_{\varepsilon,32} & Q_{\varepsilon,33} \end{pmatrix} \begin{pmatrix} E_{xjl} \\ E_{yjl} \\ E_{zjl} \end{pmatrix}, \tag{15}$$

where $\mathbf{Q}_\varepsilon$ is a matrix defined as (written without matrix indices)

$$\mathbf{Q}_\varepsilon = \begin{pmatrix} \lfloor\lceil\varepsilon_{11}\rceil\rfloor & 0 & 0 \\ 0 & \lceil\lfloor\varepsilon_{22}\rfloor\rceil & 0 \\ 0 & 0 & [\![\varepsilon_{33}]\!] \end{pmatrix}. \tag{16}$$

We noticed that the matrix $\mathbf{Q}_\varepsilon$ without any factorization takes the form $\mathbf{Q}_\varepsilon = \mathrm{diag}\left(\llbracket\varepsilon_{11}\rrbracket, \llbracket\varepsilon_{22}\rrbracket, \llbracket\varepsilon_{33}\rrbracket\right)$. Clearly, the Li's correct factorization for crossed surface-relief gratings brings faster convergence than in the the case without any factorization.

Previous Fourier analysis can also be done for equations (6)–(8) representing the proper factorization for the permeability tensor, resulting equations are similar to Maxwell's equations with permeabilities due to symmetries of Maxwell's equations.

Next procedure is straightforward, we have to eliminate variables E_z and H_z, after that we obtain the following equations (written in a compact matrix form)

$$\frac{k_0}{\mathrm{i}}\partial_z \begin{pmatrix} \mathbf{E}_x \\ \mathbf{E}_y \end{pmatrix} = \mathbf{F} \begin{pmatrix} \mathbf{H}_x \\ \mathbf{H}_y \end{pmatrix}; \quad \frac{k_0}{\mathrm{i}}\partial_z \begin{pmatrix} \mathbf{H}_x \\ \mathbf{H}_y \end{pmatrix} = \mathbf{G} \begin{pmatrix} \mathbf{E}_x \\ \mathbf{E}_y \end{pmatrix}, \tag{17}$$

where matrices

$$\mathbf{F} = \begin{pmatrix} \boldsymbol{\alpha}\llbracket\varepsilon_{33}\rrbracket^{-1}\boldsymbol{\beta} & -\boldsymbol{\alpha}\llbracket\varepsilon_{33}\rrbracket^{-1}\boldsymbol{\alpha} + k_0^2\lceil\lfloor\mu_{22}\rfloor\rceil \\ \boldsymbol{\beta}\llbracket\varepsilon_{33}\rrbracket^{-1}\boldsymbol{\beta} - k_0^2\lfloor\lceil\mu_{11}\rceil\rfloor & -\boldsymbol{\beta}\llbracket\varepsilon_{33}\rrbracket^{-1}\boldsymbol{\alpha} \end{pmatrix}, \tag{18}$$

$$\mathbf{G} = \begin{pmatrix} -\boldsymbol{\alpha}\llbracket\mu_{33}\rrbracket^{-1}\boldsymbol{\beta} & \boldsymbol{\alpha}\llbracket\mu_{33}\rrbracket^{-1}\boldsymbol{\alpha} - k_0^2\lceil\lfloor\varepsilon_{22}\rfloor\rceil \\ -\boldsymbol{\beta}\llbracket\mu_{33}\rrbracket^{-1}\boldsymbol{\beta} + k_0^2\lfloor\lceil\varepsilon_{11}\rceil\rfloor & \boldsymbol{\beta}\llbracket\mu_{33}\rrbracket^{-1}\boldsymbol{\alpha} \end{pmatrix}. \tag{19}$$

In the above, matrices $\boldsymbol{\alpha}$ and $\boldsymbol{\beta}$ are the short-hand notation for $(\alpha)_{mn,jl} = \alpha_m\delta_{mj}\delta_{nl}$ and $(\beta)_{mn,jl} = \beta_n\delta_{mj}\delta_{nl}$, $\llbracket\varepsilon\rrbracket$ is the generic element of the 4D matrix $\varepsilon_{mn,jl}$, as previously noted. let us now study truncation of matrices. The size of matrices $\boldsymbol{\alpha}$, $\boldsymbol{\beta}$, $\llbracket\rrbracket$, $\lfloor\lceil\rceil\rfloor$, $\lceil\lfloor\rfloor\rceil$ is $n_{xy}\times n_{xy}$, so the size of matrices $\mathbf{F}$ and $\mathbf{G}$ is $2n_{xy}\times 2n_{xy}$. Note that a possible way to invert a 4D matrix $M^{(4D)}_{mn,jl}$ $(m, j = 0, \ldots, 2N_x;\ n, l = 0, \ldots, 2N_y)$ is by constructing the corresponding 2D matrix $M^{(2D)}_{u,v}$ $(u, v = 1, \ldots, n_{xy})$ with $u = m(2N_y+1)+n+1$ and $v = j(2N_y+1)+l+1$.

2.2.2 Normal vector method (NVM)

According to Fourier factorization rules, discussed in the previous section 2.2.1, the Fourier coefficients of the displacement vector components can be factorized, if we decompose displacement vector to the parallel and normal component to a material interface [18].

Parallel and normal components of the electric field are used to satisfy Li's factorization rules at a material interface, but clearly the normal vector (NV) field must be given in a whole grating period (the NV must be continuous and smooth). However, the setting of the NV field is not unique.

First, let us look at the idea of the NVM. For simplicity of the explanation, we assume non-magnetic isotropic material. In case of isotropic material, the displacement vector $\boldsymbol{D}$ can be easily separated to a normal and a tangent component to the structure profile

$$\boldsymbol{D} = \varepsilon\boldsymbol{E} = \varepsilon\boldsymbol{E}_T + \varepsilon\boldsymbol{E}_N. \tag{20}$$

If we introduce a unit vector $\boldsymbol{N}$, normal to the grating profile, the normal component of the electric field vector can be defined as $\boldsymbol{E}_N = \boldsymbol{N}(\boldsymbol{N}\cdot\boldsymbol{E})$, the tangent component is then defined as $\boldsymbol{E}_T = \boldsymbol{E} - \boldsymbol{E}_N$.

We know from the previous analysis in section 2.2.1 that the term $\varepsilon \boldsymbol{E}_T$ is discontinuous and the term $\varepsilon \boldsymbol{E}_N$ is continuous, so after transformation into the Fourier domain, the term $\varepsilon \boldsymbol{E}_T$ must be calculated using Laurent's rule and the term $\varepsilon \boldsymbol{E}_N$ must be calculated using inverse rule.

$$\boldsymbol{D} = [\![\varepsilon]\!]\, \boldsymbol{E}_T + [\![1/\varepsilon]\!]^{-1} \boldsymbol{E}_N = [\![\varepsilon]\!]\, [\boldsymbol{E} - \boldsymbol{N}(\boldsymbol{N} \cdot \mathbf{E})] + [\![1/\varepsilon]\!]^{-1} [\boldsymbol{N}(\boldsymbol{N} \cdot \boldsymbol{E})]. \tag{21}$$

Next, we introduce a square matrix denoted $(\boldsymbol{NN})$ whose elements are given by $(\boldsymbol{NN})_{i,j} = N_i N_j$, the previous equation leads to

$$\boldsymbol{D} = [\![\varepsilon]\!]\, \boldsymbol{E} + \left([\![\varepsilon]\!] - \left[\!\!\left[\frac{1}{\varepsilon}\right]\!\!\right]^{-1} \right) [\![\boldsymbol{NN}]\!]\, \boldsymbol{E}. \tag{22}$$

Relation between the electric displacement vector $\boldsymbol{D}$ and the electric intensity vector $\boldsymbol{E}$ can be written in a compact form $\boldsymbol{D} = \mathbf{Q}_\varepsilon \boldsymbol{E}$ where matrix $\mathbf{Q}_\varepsilon$ is given by

$$\mathbf{Q}_\varepsilon = [\![\varepsilon]\!] - \left([\![\varepsilon]\!] - \left[\!\!\left[\frac{1}{\varepsilon}\right]\!\!\right]^{-1} \right) [\![\boldsymbol{NN}]\!], \tag{23}$$

finally, the matrix $\mathbf{Q}_\varepsilon$ takes the form

$$\mathbf{Q}_\varepsilon = \begin{pmatrix} [\![\varepsilon]\!] - \boldsymbol{\Delta} \left[\!\left[N_x^2\right]\!\right] & -\boldsymbol{\Delta} [\![N_x N_y]\!] & -\boldsymbol{\Delta} [\![N_x N_z]\!] \\ -\boldsymbol{\Delta} [\![N_x N_y]\!] & [\![\varepsilon]\!] - \boldsymbol{\Delta} \left[\!\left[N_y^2\right]\!\right] & -\boldsymbol{\Delta} [\![N_y N_z]\!] \\ -\boldsymbol{\Delta} [\![N_x N_z]\!] & -\boldsymbol{\Delta} [\![N_y N_z]\!] & [\![\varepsilon]\!] - \boldsymbol{\Delta} \left[\!\left[N_z^2\right]\!\right] \end{pmatrix}, \tag{24}$$

where $\boldsymbol{\Delta} = [\![\varepsilon]\!] - \left[\!\left[\frac{1}{\varepsilon}\right]\!\right]^{-1}$. Since we assume only 2D periodicity, $N_z = 0$:

$$\mathbf{Q}_\varepsilon = \begin{pmatrix} [\![\varepsilon]\!] - \boldsymbol{\Delta} \left[\!\left[N_x^2\right]\!\right] & -\boldsymbol{\Delta} [\![N_x N_y]\!] & 0 \\ -\boldsymbol{\Delta} [\![N_x N_y]\!] & [\![\varepsilon]\!] - \boldsymbol{\Delta} \left[\!\left[N_y^2\right]\!\right] & 0 \\ 0 & 0 & [\![\varepsilon]\!] \end{pmatrix}. \tag{25}$$

After elimination of variables E_z and H_z, we obtain the same matrix (18) and new matrix $\mathbf{G}$, the matrix $\mathbf{G}$ is defined as

$$\mathbf{G} = \begin{pmatrix} -\boldsymbol{\alpha\beta} + \mu k_0^2 \boldsymbol{\Delta} [\![N_x N_y]\!] & \boldsymbol{\alpha}^2 - \mu k_0^2 [\![\varepsilon]\!] + \mu k_0^2 \boldsymbol{\Delta} \left[\!\left[N_y^2\right]\!\right] \\ \mu k_0^2 [\![\varepsilon]\!] - \mu k_0^2 \boldsymbol{\Delta} \left[\!\left[N_x^2\right]\!\right] - \boldsymbol{\beta}^2 & \boldsymbol{\beta\alpha} - \mu k_0^2 \boldsymbol{\Delta} [\![N_y N_x]\!] \end{pmatrix}. \tag{26}$$

The sizes of the submatrices are the same as in Eqs. (18) and (19). The solution is then given by the eigenvalue equation (27).

2.3 Solution of the eigenvalue equation — aRCWA mode solver

Let us now derive the eigenvalue equation of the aRCWA method. We assume here that we have matrices $\mathbf{F}$ (18) and $\mathbf{G}$ either (19) or (26) or (??). A combination of Eqs. (17) finally gives the eigenvalue equation

$$\left(\mathbf{FG} - k_0^2 \gamma^2\right) \begin{pmatrix} \mathbf{E}_x \\ \mathbf{E}_y \end{pmatrix} = 0. \tag{27}$$

The solution of (27) is a set of eigenvalues γ and the corresponding eigenvectors $(\mathbf{E}_x, \mathbf{E}_y)^T$ (electric part of the eigenvectors). Magnetic part of the eigenvectors is easily given by

$(\mathbf{H}_x, \mathbf{H}_y)^T = \mathbf{G}(\mathbf{E}_x, \mathbf{E}_y)^T 1/(k_0\gamma)$. The modal expansions of the total field in a structure layer (p) can be written as

$$E_\sigma(r) = \sum_{m,n,q} \left[u_q \exp(\mathrm{i}\gamma_q z) + d_q \exp(-\mathrm{i}\gamma_q z)\right] \exp\left[\mathrm{i}\left(\alpha_m x + \beta_n y\right)\right] E_{\sigma mnq}, \tag{28}$$

$$H_\sigma(r) = \sum_{m,n,q} \left[u_q \exp(\mathrm{i}\gamma_q z) - d_q \exp(-\mathrm{i}\gamma_q z)\right] \exp\left[\mathrm{i}\left(\alpha_m x + \beta_n y\right)\right] H_{\sigma mnq}, \tag{29}$$

where $\sigma = x, y$, and u_q and d_q are the unknown amplitudes of the upward and downward modal fields. Once the eigenmodes and their propagating constants are known in each layer, we have to match the boundary conditions (see some textbook on Optics) at the interfaces to compute u_q and d_q. For computation, we use a stable matrix algorithm, e.g. S-matrix algorithm [19] or enhanced T-matrix algorithm [9] (standard T-matrix algorithm is numerically unstable). The physical quantities, that characterize how the incident field power are distributed, can be chosen according to actual needs (e.g. periodic/aperiodic RCWA, ...). We mention here only the most important quantities used in our simulations:

- diffraction efficiencies,
- modal reflectivity, modal transmissivity,
- power detector.

2.4 Absorbing layers

To simulate general aperiodic photonic structures using the RCWA method, it is necessary to insert the artificial absorbing layers between adjacent periods. Such absorbing layers must completely separate the periods and the periods then become independent. Absorbing layers must minimize backward parasitic reflections of light into the investigated structure, i.e. they do not create a reflection for any wavelength, angle, or polarization. Concerning the proper boundary conditions for the aRCWA method, they are, in fact, present in other methods (especially in FDTD and FEM methods), where "open" structures (structures in infinite space) are simulated, too. From the computational point of view, it is necessary to properly enclose the investigated structure by absorbing layers.

A perfectly matched layer (PML) [20] is an artificial "absorbing" layer used to truncate computational regions in numerical methods. The concept of PMLs, which is suitable for the aRCWA method, can be introduced in a variety of ways, using either also a complex refractive index distribution [21], a complex coordinate stretching [22], anisotropic uniaxial media [23], or a nonlinear complex coordinate transformation [1]. Further, we will focus on the nonlinear complex coordinate transformation and the anisotropic uniaxial media. We have implemented and tested both PML techniques.

2.4.1 Nonlinear complex coordinate transformation

Nonlinear complex coordinate transformation [1] is used as an efficient boundary condition of the PML type, it is designed to absorb the outgoing waves at the computational boundaries. Motivated with [1], paper [24] introduce another coordinate transformation. The figure 8 shows the coordinate transformation and its first derivative; the mathematical definition of the coordinate transform can be found in [1, 24]. Now, the computational space in the x-direction (similarly in the y-direction) is divided into three subintervals $(x_{min}$,$x_b)$, $(x_b$,$x_u)$, and $(x_u$,$x_{max})$; the absorption of the outgoing waves occurs in the first and the third interval due to the nonlinear and complex space, while the space in the second interval is linear and non-complex (see Fig. 8); therefore, the space is non-absorbing in this layer.

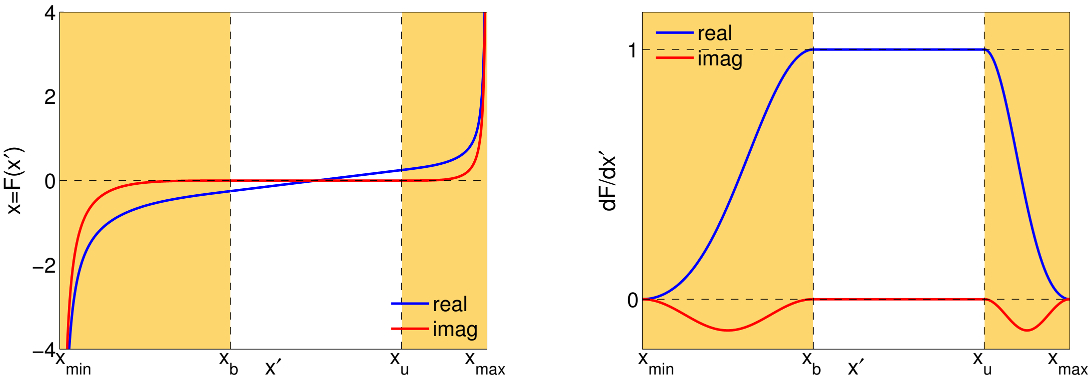

a) b)

Figure 8 A typical example of the nonlinear coordinate transformation: a) function $x = F(x')$, b) function $f(x')$ for $\gamma_{PML} = 1/(1 - \mathrm{i})$.

In order to express the matrix equations (17) in the new absorbing coordinate system (x', y'), it is necessary to know relations between partial derivatives if the old and new coordinate system $\partial/\partial x$ and $\partial/\partial x'$ and between $\partial/\partial y$ and $\partial/\partial y'$ hence in the x-direction

$$\frac{\partial}{\partial x} = \frac{\partial x'}{\partial x}\frac{\partial}{\partial x'} = \left(\frac{\partial F(x')}{\partial x'}\right)^{-1}\frac{\partial}{\partial x'} = f_{x'}\frac{\partial}{\partial x'}, \tag{30}$$

and in the y-direction

$$\frac{\partial}{\partial y} = \frac{\partial y'}{\partial y}\frac{\partial}{\partial y'} = \left(\frac{\partial F(y')}{\partial y'}\right)^{-1}\frac{\partial}{\partial y'} = f_{y'}\frac{\partial}{\partial y'}. \tag{31}$$

So it means that the formulation of the eigenvalue problem in the new coordinate system (x', y') is obtained by replacing matrices $\boldsymbol{\alpha}$ and $\boldsymbol{\beta}$ in equations (17) by the matrices $\mathbf{F}_x\boldsymbol{\alpha}$ and $\mathbf{F}_y\boldsymbol{\beta}$, where matrices $\mathbf{F}_x$ and $\mathbf{F}_y$ are Toeplitz matrices which are composed of the Fourier series elements of functions $f_{x'}$ and $f_{y'}$, respectively.

For the sake of completeness, the function $f(x')$ is given by [24, 11]

$$\begin{aligned} f(x')_{(x'_{min},x'_b)} &= \left[1 - \gamma_{PML}\sin^2\left(\frac{\pi(x'-x'_b)}{2(x'_b - x'_{min})}\right)\right]\cos^2\left(\frac{\pi(x'-x'_b)}{2(x'_b - x'_{min})}\right) \\ f(x')_{(x'_b,x'_u)} &= 1 \\ f(x')_{(x'_u,x'_{max})} &= \left[1 - \gamma_{PML}\sin^2\left(\frac{\pi(x'-x'_u)}{2(x'_{max} - x'_u)}\right)\right]\cos^2\left(\frac{\pi(x'-x'_u)}{2(x'_{max} - x'_u)}\right) \end{aligned}, \tag{32}$$

where $\gamma_{PML} = 1/(1+\mathrm{i})$;[1] the function $f(y')$ is given in the same way. For the numerical implementation of the aRCWA method, the functions $f(x')$ and $f(y')$ must be expanded in the 2D Fourier series. However, for some special purposes, $\gamma_{PML} \in \mathbb{R}$ is also applicable, e.g. when the aRCWA method is used as a eigenmode solver.

2.4.2 Uniaxial perfectly matched layers

It has also been discovered [23] that the reflection less properties of a material can be achieved if the material is assumed to be diagonally anisotropic, hence they are called as uniaxial perfectly matched layers. Artificial material properties of a such layer are selected so that the interface between the absorbing layer and free space shows up no reflections. Its permeability and permittivity tensors can be written as $\varepsilon = \varepsilon_0\varepsilon_r\Psi$ and $\mu = \mu_0\mu_r\Psi$, where

$$\Psi = \begin{pmatrix} a & 0 & 0 \\ 0 & b & 0 \\ 0 & 0 & c \end{pmatrix}, \tag{33}$$

where a, b, and c are constants. In order to damp all transmitted radiation, the paper [23] shows that the values a, b, and c are not independent. They are interconnected with

$$a = b = \frac{1}{c}. \tag{34}$$

Thus, the PML layer can be characterized by one complex number $\alpha = \alpha' + \mathrm{i}\alpha''$. When $\alpha, \beta > 0$, the transmitted wave will be damped in the anisotropic medium. For the computation, the PML absorbers are best defined as is in Fig. 9. Absorbers type 1 and type 2 only consider the case of a wave incident on a single planar boundary. However, an ambiguity occurs in the corner regions where there is more than one normal interface boundary. Within these regions, a more generalized constitutive relationship is necessary (see [23]). In brief [25], anisotropic parameters for type 2 absorbers are $\mu_{11} = \mu_{33} = \varepsilon_{11} = \varepsilon_{33} = \alpha$ and $\mu_{22} = \varepsilon_{22} = 1/\alpha$. For type 1 absorbers, $\mu_{22} = \mu_{33} = \varepsilon_{22} = \varepsilon_{33} = \alpha$ and $\mu_{11} = \varepsilon_{11} = 1/\alpha$. For type 3 absorbers, $\mu_{11} = \mu_{22} = \varepsilon_{11} = \varepsilon_{22} = 1$ and $\mu_{33} = \varepsilon_{33} = \alpha^2$. In our simulations, typical values of constant α are chosen between $1(1+\mathrm{i})$ and $5(1+\mathrm{i})$.

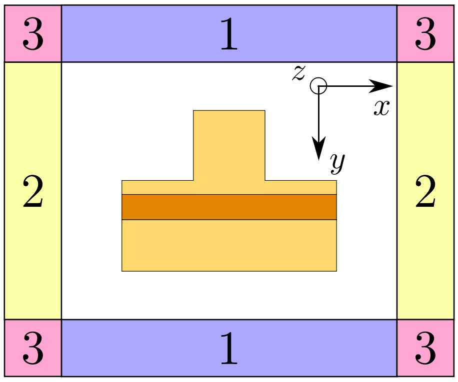

Figure 9 Arrangement of absorbing layers in the 2D computation window.

We have implemented and successfully applied both these types of boundary condition, as will be demonstrated in section 4. Via a detailed testing we have found practically equal performance of these two types of boundaries.

2.5 Adaptive spatial resolution technique

The adaptive spatial resolution (ASR) technique [26] is widely used in the RCWA method to reduce the Gibbs phenomenon (overshooting of the values) around the discontinuities of the permittivity thereby to improve the convergence of the Fourier series, finally improving the accuracy of the computation result.

[1] our previous research has shown that $\gamma_{PML} = 1/(1+\mathrm{i})$ is the most efficient value

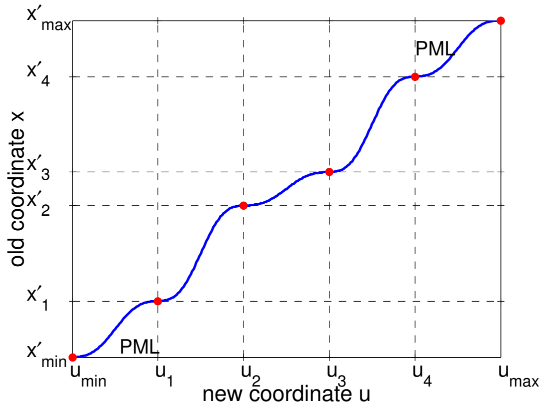

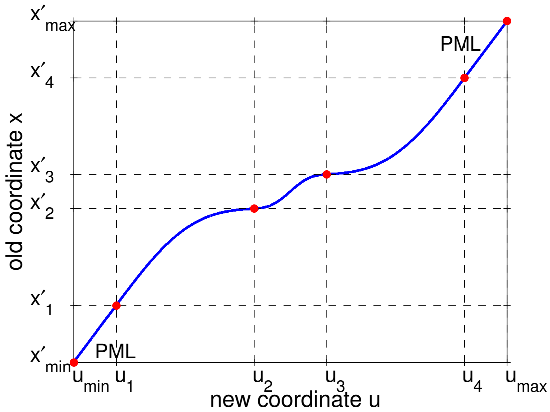

Figure 10 Schematic graph of ASR transformations: a) the ASR transformation according to [27], b) the ASR transformation according to [11], the main difference between both transformation is within the PML region, in case of the ASR transformation according to [11], the transformation is chosen to be linear.

For simplicity, let us consider only transformation of coordinate x' (x with prime means that original x is taken after the application of PML — coordinate transformation) in the x', y', z space. The ASR technique is then a coordinate transformation which transforms the coordinate x' as a function of new coordinate u'; the transition points are denoted by x'_l in the x' space and by u_l in the u space. In order to proceed from $(l-1)$ to l transitions, we use the transformation function $x'_l(u)$ for the mapping between different spaces, typically of the form (see Fig. 10a)):

$$x'_l(u) = a_1 + a_2 u + \frac{a_3}{2\pi} \sin\left[2\pi \frac{u - u_{l-1}}{u_l - u_{l-1}}\right], \tag{35}$$

where

$$a_1 = \frac{u_l x'_{l-1} - u_{l-1} x'_l}{u_l - u_{l-1}}, \qquad a_2 = \frac{x'_l - x'_{l-1}}{u_l - u_{l-1}}, \qquad a_3 = G(u_l - u_{l-1}) - (x'_l - x'_{l-1}), \tag{36}$$

where G is a stretching coefficient in the interval $(0, 1\rangle$. It's choice can be used to tune and optimize the ASR performance. According to (35), there is a possibility of having different dimensions in the new (u, y', z) space than in the (x', y', z) space. The choice of coordinates in the transformed space has a direct consequence on the convergence of the Fourier series, this choice will be discussed in the end part of this subsection.

In addition, there are many ways how to choose the ASR transformation function. Motivated with [27], we have proposed another ASR transformation [11] (see Fig. 10b)). The mathematical definition of our ASR function is given in [11]. Here we require that $x'_l(u)$ leaves the former PML transformation intact, furthermore, within the PML regions, our ASR function is chosen to be linear with the slope of unity and to be smooth at both the lower and upper boundaries of the PML regions.

Typical graphs of the functions $\varepsilon(u)$ and $a(u) = h(u)\varepsilon(u)$ (transformed permittivity) are plotted in Fig. 11a). The function $a(u)$ is given by the product of permittivity function and the scaling function h which is defined as $h = \mathrm{d}x'/\mathrm{d}u$. It can be seen that the Fourier

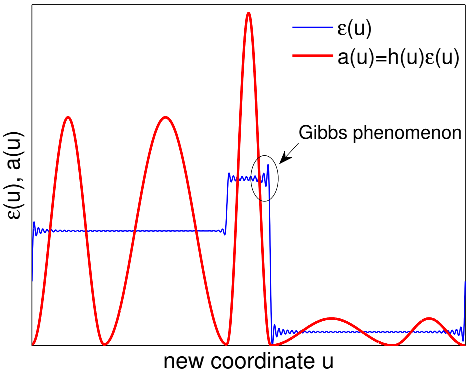

a)

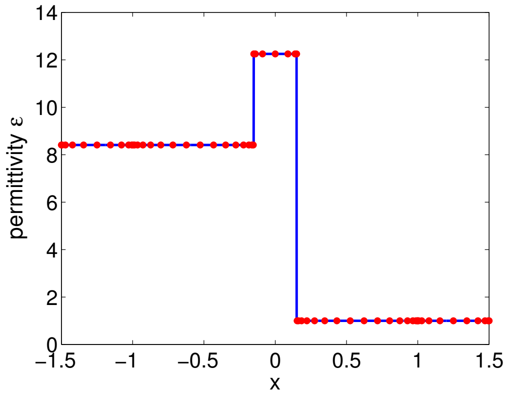

b)

Figure 11 A typical example of the ASR function: a) Step-index profile of ε with the Gibbs phenomenon at the edges is reduced using the ASR technique, b) spatial resolution is increased around the discontinuities of the permittivity.

series of the function ε contains the Gibbs phenomenon at the edges, whereas the Gibbs phenomenon is reduced in case of the function a. Because of the step-index profile of the permittivity (chosen as an example in Fig. 11) is transformed into harmonic-type profile, which is more suitable for the Fourier series, the speed of the convergence is faster than in the case without the ASR technique. Figure 11b) illustrates the simultaneous increase of the spatial resolution around the discontinuities of the permittivity.

In our case of 2D periodicity, identical coordinate transformation $y'(v)$ is placed along the y' direction. Paper [28] shows practical implementation of 2D ASR transformation. Based on the covariant form of Maxwell's equations (1) and (2), the covariant metric tensor $\sqrt{g_T}$ takes the following form:

$$\sqrt{g_T} = \begin{pmatrix} \frac{g}{h} & 0 & 0 \\ 0 & \frac{h}{g} & 0 \\ 0 & 0 & gh \end{pmatrix}, \tag{37}$$

where g and h are defined as $h = \mathrm{d}x'/\,\mathrm{d}u$, $g = \mathrm{d}y'/\,\mathrm{d}v$. As we have already shown in previous section 2.4.2, this transformation of coordinates can be easily included in uniaxial $\overleftrightarrow{\epsilon}$ and $\overleftrightarrow{\mu}$ tensors

$$\overleftrightarrow{\varepsilon} = \begin{pmatrix} \frac{g}{h}\varepsilon_{11} & 0 & 0 \\ 0 & \frac{h}{g}\varepsilon_{22} & 0 \\ 0 & 0 & gh\varepsilon_{33} \end{pmatrix}, \qquad \overleftrightarrow{\mu} = \begin{pmatrix} \frac{g}{h}\mu_{11} & 0 & 0 \\ 0 & \frac{h}{g}\mu_{22} & 0 \\ 0 & 0 & gh\mu_{33} \end{pmatrix}. \tag{38}$$

Inspired with [28], we have successfully implemented the 2D ASR transformation [29–31]. There are questions about choosing the proper value of parameter G and the choice of coordinates in the transformed space. Unfortunately no scheme exists so far to predict the optimum choice of parameters G for the ASR transformation, according to our experience, the parameter G should be close to zero (e.g. 0.01). Hence, it can be that another value leads to better results, but it is not our intention to discuss this problem in closer details now.

3 Full-anisotropic aRCWA algorithm

In order to analyse magneto-optic waveguides within our research projects, we have developed an efficient 2D numerical technique based on magneto-optic aperiodic rigorous coupled wave analysis (MOaRCWA). The artificial periodicity is imposed within a periodic 1D RCWA method, in the form of the complex transformation and / or uniaxial perfectly matched layers. Our approach, in which several key improvements relevant for the Fourier modal method approach have been implemented, is able to properly cope not only with magneto-plasmons propagation effects in corresponding nanostructures, but also with a fully general form of permittivity / permeability anisotropy. We will follow the basic idea of the paper [32], where the derivation of (periodic) full-anisotropic RCWA method is given. Our implementation for the aRCWA is original and will be subsequently published.

Magneto-optic Fourier modal method (or MOaRCWA) simulations are demonstrated in section 4.2 where we analyse nonreciprocal magnetoplasmonic waveguides formed with InSb material, applicable as one-way structures in the THz frequency range.

3.1 Eigenvalue equation

The mathematical description of the method, we focus only on the Maxwell's equation (1), where there is a permittivity function ε. The factorization analysis of terms in Maxwell's equation (2) is similar to factorization analysis of (1), and will not be shown here, due to simplicity. After expanding of Maxwell's equation (1), we obtain the system of equations

$$\partial_2 H_3 - \partial_3 H_2 = -\mathrm{i}k_0 \left(\varepsilon_{11} E_1 + \varepsilon_{12} E_2 + \varepsilon_{13} E_3\right), \quad (39)$$
$$\partial_3 H_1 - \partial_1 H_3 = -\mathrm{i}k_0 \left(\varepsilon_{21} E_1 + \varepsilon_{22} E_2 + \varepsilon_{23} E_3\right), \quad (40)$$
$$\partial_1 H_2 - \partial_2 H_1 = -\mathrm{i}k_0 \left(\varepsilon_{31} E_1 + \varepsilon_{32} E_2 + \varepsilon_{33} E_3\right). \quad (41)$$

Here, we switch to use 1, 2, 3 instead of x, y, z to denote the field components. Our method is based on the 1D-periodic RCWA method [32], where the electromagnetic field components and permittivity and permeability tensor elements are expanded into Floquet-Fourier series. Due to numerical truncation of the Fourier series, Maxwell's equations must be correctly converted into linear algebraic systems in the discrete Fourier space. According to [32], the system of equations (39)–(41) can be rewritten as

$$\partial_2 H_3 - \partial_3 H_2 = -\mathrm{i}k_0 \left(Q_{\varepsilon,11} E_1 + Q_{\varepsilon,12} E_2 + Q_{\varepsilon,13} E_3\right),$$
$$\partial_3 H_1 - \partial_1 H_3 = -\mathrm{i}k_0 \left(Q_{\varepsilon,21} E_1 + Q_{\varepsilon,22} E_2 + Q_{\varepsilon,23} E_3\right),$$
$$\partial_1 H_2 - \partial_2 H_1 = -\mathrm{i}k_0 \left(Q_{\varepsilon,31} E_1 + Q_{\varepsilon,32} E_2 + Q_{\varepsilon,33} E_3\right).$$

where the matrix $Q_{\varepsilon,ik}$ (dimension 3×3) is defined as (after applying both the ASR technique h and the anisotropic PML to both $\overleftrightarrow{\varepsilon}$ and $\overleftrightarrow{\mu}$)

$$\mathbf{Q}_\varepsilon = \begin{pmatrix} \left[\!\left[\frac{h}{\varepsilon'_{11}}\right]\!\right]^{-1} & \left[\!\left[\frac{h}{\varepsilon'_{11}}\right]\!\right]^{-1}\left[\!\left[\frac{h\varepsilon'_{12}}{\varepsilon'_{11}}\right]\!\right] & \left[\!\left[\frac{h}{\varepsilon'_{11}}\right]\!\right]^{-1}\left[\!\left[\frac{h\varepsilon'_{13}}{\varepsilon'_{11}}\right]\!\right] \\ \left[\!\left[\frac{h\varepsilon'_{21}}{\varepsilon'_{11}}\right]\!\right]\left[\!\left[\frac{h}{\varepsilon'_{11}}\right]\!\right]^{-1} & \left[\!\left[\frac{h\varepsilon'_{21}}{\varepsilon'_{11}}\right]\!\right]\left[\!\left[\frac{h}{\varepsilon'_{11}}\right]\!\right]^{-1}\left[\!\left[\frac{h\varepsilon'_{12}}{\varepsilon'_{11}}\right]\!\right] + \left[\!\left[h\left(\varepsilon'_{22} - \frac{\varepsilon'_{21}\varepsilon'_{12}}{\varepsilon'_{11}}\right)\right]\!\right] & \left[\!\left[\frac{h\varepsilon'_{21}}{\varepsilon'_{11}}\right]\!\right]\left[\!\left[\frac{h}{\varepsilon'_{11}}\right]\!\right]^{-1}\left[\!\left[\frac{h\varepsilon'_{13}}{\varepsilon'_{11}}\right]\!\right] + \left[\!\left[h\left(\varepsilon'_{23} - \frac{\varepsilon'_{21}\varepsilon'_{13}}{\varepsilon'_{11}}\right)\right]\!\right] \\ \left[\!\left[\frac{h\varepsilon'_{31}}{\varepsilon'_{11}}\right]\!\right]\left[\!\left[\frac{h}{\varepsilon'_{11}}\right]\!\right]^{-1} & \left[\!\left[\frac{h\varepsilon'_{31}}{\varepsilon'_{11}}\right]\!\right]\left[\!\left[\frac{h}{\varepsilon'_{11}}\right]\!\right]^{-1}\left[\!\left[\frac{h\varepsilon'_{12}}{\varepsilon'_{11}}\right]\!\right] + \left[\!\left[h\left(\varepsilon'_{32} - \frac{\varepsilon'_{31}\varepsilon'_{12}}{\varepsilon'_{11}}\right)\right]\!\right] & \left[\!\left[\frac{h\varepsilon'_{31}}{\varepsilon'_{11}}\right]\!\right]\left[\!\left[\frac{h}{\varepsilon'_{11}}\right]\!\right]^{-1}\left[\!\left[\frac{h\varepsilon'_{13}}{\varepsilon'_{11}}\right]\!\right] + \left[\!\left[h\left(\varepsilon'_{33} - \frac{\varepsilon'_{31}\varepsilon'_{13}}{\varepsilon'_{11}}\right)\right]\!\right] \end{pmatrix}.$$

Resulting matrix $\mathbf{R}_\mu$ (dimension 3×3) for permeability tensor $\overleftrightarrow{\mu}$ is similar to the matrix $\mathbf{Q}_\varepsilon$. After eliminating electromagnetic field components E_2 and H_2 , we get the eigenvalue equation: $\mathbf{A}(\mathbf{E}_3, \mathbf{H}_3, \mathbf{H}_1, \mathbf{E}_1)^{\mathrm{T}} = \lambda(\mathbf{E}_3, \mathbf{H}_3, \mathbf{H}_1, \mathbf{E}_1)^{\mathrm{T}}$ (λ denotes eigenvalues), where matrix $\mathbf{A}$ (dimension 4×4) is given by

$$\mathbf{A} = \begin{pmatrix} -\mathbf{R}_{\mu,12}\mathbf{R}^{-1}_{\mu,22}\boldsymbol{\alpha} & -k_0\mathbf{R}_{\mu,12}\mathbf{R}^{-1}_{\mu,22}\mathbf{R}_{\mu,23} + k_0\mathbf{R}_{\mu,13} & k_0\mathbf{R}_{\mu,11} - k_0\mathbf{R}_{\mu,12}\mathbf{R}^{-1}_{\mu,22}\mathbf{R}_{\mu,21} & \mathbf{0} \\ k_0\mathbf{Q}_{12}\mathbf{Q}^{-1}_{\varepsilon,22}\mathbf{Q}_{23} - k_0\mathbf{Q}_{\varepsilon,13} & -\mathbf{Q}_{\varepsilon,12}\mathbf{Q}^{-1}_{22}\boldsymbol{\alpha} & \mathbf{0} & -k_0\mathbf{Q}_{\varepsilon,11} + k_0\mathbf{Q}_{\varepsilon,12}\mathbf{Q}^{-1}_{\varepsilon,22}\mathbf{Q}_{\varepsilon,21} \\ -k_0\mathbf{Q}_{\varepsilon,32}\mathbf{Q}^{-1}_{\varepsilon,22}\mathbf{Q}_{\varepsilon,23} + k_0\mathbf{Q}_{\varepsilon,33} - \frac{1}{k_0}\boldsymbol{\alpha}\mathbf{R}^{-1}_{\mu,22}\boldsymbol{\alpha} & \mathbf{Q}_{\varepsilon,32}\mathbf{Q}^{-1}_{\varepsilon,22}\boldsymbol{\alpha} - \boldsymbol{\alpha}\mathbf{R}^{-1}_{\mu,22}\mathbf{R}_{\mu,23} & -\boldsymbol{\alpha}\mathbf{R}^{-1}_{\mu,22}\mathbf{R}_{\mu,21} & k_0\mathbf{Q}_{\varepsilon,31} - k_0\mathbf{Q}_{\varepsilon,32}\mathbf{Q}^{-1}_{\varepsilon,22}\mathbf{Q}_{\varepsilon,21} \\ \mathbf{R}_{\mu,32}\mathbf{R}^{-1}_{\mu,3222}\boldsymbol{\alpha} - \boldsymbol{\alpha}\mathbf{Q}^{-1}_{\varepsilon,22}\mathbf{Q}_{\varepsilon,23} & k_0\mathbf{R}_{\mu,32}\mathbf{R}^{-1}_{\mu,22}\mathbf{R}_{\mu,23} - k_0\mathbf{R}_{\mu,33} + \frac{1}{k_0}\boldsymbol{\alpha}\mathbf{Q}^{-1}_{\varepsilon,22}\boldsymbol{\alpha} & -k_0\mathbf{R}_{\mu,31} + k_0\mathbf{R}_{\mu,32}\mathbf{R}^{-1}_{\mu,22}\mathbf{R}_{\mu,21} & -\boldsymbol{\alpha}\mathbf{Q}^{-1}_{\varepsilon,22}\mathbf{Q}_{\varepsilon,21} \end{pmatrix}, \qquad (42)$$

where $\boldsymbol{\alpha}$ is the diagonal matrix with elements $\alpha_n = n2\pi/\Lambda_x$, $k_0 = 2\pi/\lambda_0$ and λ_0 is the vacuum wavelength, and Λ_x is the artificial period of the system. Integer n is taken from the interval $[-N, N]$, where the integer N describes the truncation order; hence the size of all submatrices is $(2N + 1)$ square and the size of the matrix $\mathbf{A}$ is $4(2N + 1)$ square.

After obtaining eigenvalues and eigenvectors in each layer, boundary conditions are matched on each boundary (e.g. with the S-matrix algorithm).

Here, we have derived (implemented) a general form of the eigenvalue equation which allows dealing with fully anisotropic medium described by a general form of permittivity and/or permeability tensor.

3.2 Eigenvalue equation: case of transversal configuration

Now we are going to simplify the general eigenvalue equation (42), derived above. The eigenvalue equation (42) is derived for general tensors $\overleftrightarrow{\varepsilon}$ and $\overleftrightarrow{\mu}$. In the presence of the external magnetic field, there are three possible magneto-optic (MO) configurations, transversal (or Voigt), longitudinal (Faraday), and polar configuration.

Next, we focus on transversal (Voigt) magneto-optic configuration (see Fig. 12a)), the tensor $\overleftrightarrow{\varepsilon}$ takes the form of

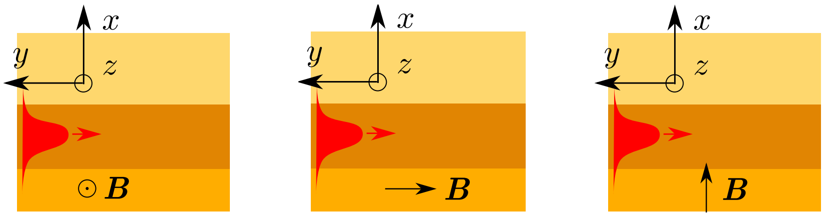

Figure 12 Schematic drawing of three possible MO waveguide configurations: a) transversal (Voigt), b) longitudinal (Faraday), c) polar configuration.

$$\overleftrightarrow{\varepsilon} = \begin{pmatrix} \varepsilon_{11} & \varepsilon_{12} & 0 \\ -\varepsilon_{12} & \varepsilon_{22} & 0 \\ 0 & 0 & \varepsilon_{33} \end{pmatrix}.$$

In that case, the general eigenvalue equation (42) can be simplified according to TM/TE polarization [33]. In case of TM polarization, reduced eigenvalue equation leads to

$$\begin{pmatrix} -\mathbf{Q}_{\varepsilon,12}\mathbf{Q}_{\varepsilon,22}^{-1}\boldsymbol{\alpha} & -k_0\mathbf{Q}_{\varepsilon,11} + k_0\mathbf{Q}_{\varepsilon,12}\mathbf{Q}_{\varepsilon,22}^{-1}\mathbf{Q}_{\varepsilon,21} \\ -k_0\mathbf{R}_{\mu,33} + \frac{1}{k_0}\boldsymbol{\alpha}\mathbf{Q}_{\varepsilon,22}^{-1}\boldsymbol{\alpha} & -\boldsymbol{\alpha}\mathbf{Q}_{\varepsilon,22}^{-1}\mathbf{Q}_{\varepsilon,21} \end{pmatrix} \begin{pmatrix} \mathbf{H}_3 \\ \mathbf{E}_1 \end{pmatrix} = \lambda \begin{pmatrix} \mathbf{H}_3 \\ \mathbf{E}_1 \end{pmatrix},$$

and the TE eigenvalue equation is given by

$$\begin{pmatrix} \mathbf{0} & k_0\mathbf{R}_{\mu,11} \\ k_0\mathbf{Q}_{\varepsilon,33} - \frac{1}{k_0}\boldsymbol{\alpha}\mathbf{R}_{\mu,22}^{-1}\boldsymbol{\alpha} & \mathbf{0} \end{pmatrix} \begin{pmatrix} \mathbf{E}_3 \\ \mathbf{H}_1 \end{pmatrix} = \lambda \begin{pmatrix} \mathbf{E}_3 \\ \mathbf{H}_1 \end{pmatrix}.$$

The eigenvalue equation for TE polarization may be further simplified, but we will mainly focus on TM polarization case. In this case, the eigenvalue problem of a matrix size $4(2N+1)$ square (for N diffraction orders) is reduced to the eigenvalue problem of a matrix size $2(2N+1)$ square, i.e. twice. The corresponding calculation time and memory consumption is about one-eighth compared with the full-anisotropic RCWA.

4 Numerical analysis of selected advanced problems

This chapter is devoted to the demonstration of the applicability of the (a)RCWA method to the analysis of various photonic / plasmonic nanostructures as we studied in the previous years. For the purpose of this text, only several examples were chosen, the number of examples has been much larger. Here, we start with the application of the 2D-periodic RCWA method to the localized surface plasmons based sensors. Then we analyse non-reciprocal magnetoplasmonic waveguides using the magneto-optic aRCWA method (see Ch. 3). Finally, we demonstrate the aRCWA method as a fully 3D effective tool for treating photonic / plasmonic nanostructures particularly, in this case PhC nanocavities with large Q.

These examples presented further, in fact, comprise an representative selection of a much larger portfolio of simulations, we have successfully performed in previous years, using our (a)RCWA tools. Specifically, I was deeply involved in the Czech Science Foundation project Physics and advanced simulations of photonic and plasmonic structures (2010–2013) where both the main tools presented in this thesis as well as applications were achieved. Concerning the simulations for the applications, we performed extensive studies and simulations in such areas as: photonic magnetooptic structures with nonreciprocal properties (such as InSb MO guides presented in section 4.2), advanced plasmonic nanostructures for guided-wave applications (such as hybrid plasmonic waveguides), novel 3D resonant nanostructures (such as photonic crystal nanocavities with high figures of merit), plasmon-based sub-wavelength structures and negative-index metamaterials (simulations of various types of plasmonic metamaterials, such as fishnets, using (a)RCWA, not presented in this text), and investigation of light interaction in photonic crystals (simulations of various types of advanced photonic crystals, including metallo-dielectric ones, performed with adapted (a)RCWA — not presented in this text).

4.1 Sensors based on localized surface plasmon (LSP)

This section is devoted to our recent modelling activities in optical (bio) sensors based on surface plasmon resonance for the detection of chemical and biochemical species mainly, within the Czech Science Foundation (GACR) project P205/12/G118. Surface plasmons (SPs) are coherent oscillations of free electrons at the boundaries between metal and dielectric which are often categorized into two classes: propagating surface plasmons (PSPs) and localized surface plasmons (LSPs). While PSPs are propagating electromagnetic waves at an interface, in case of LSP, there is no propagating wave at surface, but instead enhanced surface field near the particle's surface; this enhancement falls off quickly with distance from the surface. Plasmon resonant frequencies of PSPs and LSPs are highly sensitive to slight refractive index changes (caused by a change of the concentration of a measured medium, as e.g. bacteria, chemical compounds, . . .) in the adjacency of noble metal nanoparticles, making PSPs LSPs attractive for the development of plasmonic biosensors [34]. Compared to SPPs and/or LSPs exhibit considerably lower refractive index sensitivity corresponding to bulk refractive index changes; however, the resolution corresponding to surface refractive index changes is comparable [35] due to higher localization of the electromagnetic field at the interface between dielectric and metal. Potential benefits of LSP sensor platform are high localization, enhanced efficiency and faster response.

Next section demonstrates the use of the 2D-periodic RCWA method as an efficient tool to simulate LSP-based-sensors.

4.1.1 LSP-based-sensors on an array of random nanodisks

This section summarizes the main results of our recent paper [36]. In this work, we studied the optical response of Fano resonance resulting from the interference between localized surface plasmons on a random array of gold nanoparticles on a glass substrate and reflection of light at the boundary of the glass substrate. In this complex project, combining theoretical simulations and experiments, our role was in RCWA simulations. We highlight these here. To remind the reader, the Fano resonances [37] arising from the interference between a non-radiative mode and a continuum of radiative electromagnetic waves, the interference produces the asymmetric line-shape.

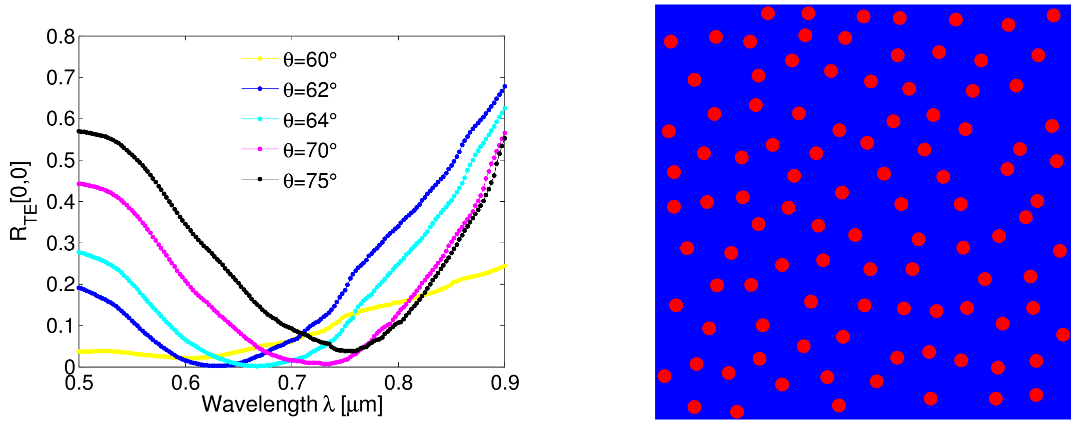

a) b)

Figure 13 a) Reflection spectra of the random nanodisk array with different incident angles θ, as calculated with our modified RCWA technique, b) "random" distribution of nanodisks in a super cell having a dimension of 3×3 μm, positions of nanodisks were taken from an AFM scan.

A model structure consists of an array of random gold nanodisks on glass substrate, so there is a question how to use RCWA technique, since in principle, the RCWA technique is able to analyse periodic structures only. Due to this fact, we developed a new original approach enabling the simulation/treatment for such cases. The actual random positions of nanodisks in a super-cell were taken from an AFM scan of realized samples (see Fig. 13b).

We designed a super cell having a dimension of 3×3 μm, containing 99 gold nanodisks supported on a glass substrate, and surrounded by water ($n_{\text{water}} = 1.33$). Proper dimension of the artificial period was tested numerically to ensure the conservation of statistics. To ensure accurate results (determined via numerical tests), we have finally divided the supercell into 2044×2044 parts (i.e., for a nanodisk of 110-nm diameter, typically 70 divisions were considered) and used truncation order $N_x = N_y = 23$ within the method (i.e., $(2N_x + 1)^2 = 2209$ modes included in the calculation), with the Li's factorization technique (see Sec. 2.2.1).

Figure 13a) shows reflection spectra of the random nanodisk array with different incidence angles θ. Note that positions of characteristic dips are shifted to longer wavelengths with increasing angle of incidence.

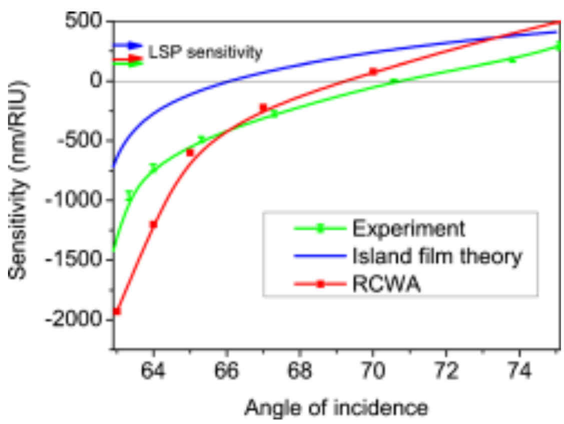

Figure 14 Angular dependence of the sensitivity to refractive index changes obtained using the modified RCWA, island film theory [38], and experiment; the sensitivity of LSP is marked by arrows in the upper part of the figure, figure is taken from [36].

Figure 14 shows angular dependence of the sensitivity to refractive index changes of the surrounding medium $\Delta n_{\mathrm{water}} = 0.01$. As illustrated in Fig. 14, for a smaller/larger angle of incidence, an increase in the refractive index shifts the resonant feature to shorter/longer wavelengths. Such an abnormal sensor behaviour is caused by the combination of the sensitivity of LSP to the refractive index (which is always positive) and the sensitivity of reflection of light (from glass substrate) to the refractive index which may be both positive and negative. Moreover, it can be seen from figure 14 that RCWA simulation agrees best with the experimental results. Also, we have implemented an approximate technique based on the effective medium approach, namely island film theory [38] with reasonable agreement, too.

4.2 Magneto-optic waveguides

The second example deals with the application of the magneto-optic (MO) aperiodic rigorous coupled wave analysis (MOaRCWA) method to magneto-optic waveguides simulations. Among surface waves constrained and propagating along media interfaces of various photonic or plasmonic nanostructures, recently, magnetoplasma surface waves; or magnetoplasmons (MSP); generated with an external magnetic field (mainly in the transverse, or Voigt configuration), have found an increasing scientific interest in many areas ranging from sensors, nonreciprocal guiding systems, to metamaterials, due to their novel properties [39]. In order to properly analyse such MSP phenomena, appropriate simulation tools are necessary. For that purpose, we have developed an efficient 2D numerical technique based on the MOaRCWA method, the description of the method is given in Ch. 3.

Based on previous investigation of one-way waveguides consisting of metal / MO photonic crystal interface [40], we have focused on the structures containing interface InSb / dielectric interface [41]. Our work has been partially motivated by recent investigation of Au / dielectric / InSb sandwiched guiding structures [42]. This completed research is ready for the submission to an impacted journal.

4.2.1 InSb magneto-optic medium

If the magnetic field or the magnetization of a medium are aligned perpendicularly to the sample plane XY (see Fig. 15), this configuration is called transversal (Voigt) magneto-optic configuration (another configurations are briefly discussed in Sec. 3.2). According to the MO Drude dispersion model [42], with the damping taken into account, the frequency dependence of the relevant permittivity tensor is given as

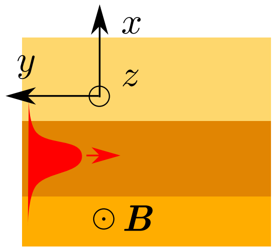

Figure 15 Transversal (Voigt) magneto-optic configuration.

$$\varepsilon = \varepsilon_\infty \begin{pmatrix} \varepsilon_{xx} & \mathrm{i}\varepsilon_{xy} & 0 \\ -\mathrm{i}\varepsilon_{xy} & \varepsilon_{xx} & 0 \\ 0 & 0 & \varepsilon_{zz} \end{pmatrix}, \tag{43}$$

where

$$\varepsilon_{xx} = 1 - \frac{\omega_p^2(\omega + \mathrm{i}\gamma)}{\omega\left[(\omega+\mathrm{i}\gamma)^2 - \omega_c^2\right]},\ \varepsilon_{xy} = \frac{\omega_p^2\omega_c}{\omega\left[(\omega+\mathrm{i}\gamma)^2 - \omega_c^2\right]},\ \varepsilon_{zz} = 1 - \frac{\omega_p^2}{\omega(\omega+\mathrm{i}\gamma)^2}, \tag{44}$$

where, ε_∞ is high-frequency limit permittivity, ω_p is the plasma frequency, γ is the collision frequency of carriers, $\omega_c = eB/m^*$ is the cyclotron frequency, e and m^* are the charge and the effective mass of electrons, respectively. Typically, the strength of the magnetic field B reaches a few Tesla.

The following parameters of InSb material as the input into the model at room temperature and magnetic field $B = 1$ T were chosen: $\varepsilon_\infty = 15.68$, $\omega_p = 12.6$ THz, $\gamma = (0.1\pi)$ THz, and $\omega_c = 12.56$ THz.

4.2.2 One-way plasmonic waveguides operating at the THz range

For photonics to become a realistic alternative to electronics compact integrated optical analog of one-way electronic devices such as diodes and transistors, are needed. Most of the photonic nonreciprocal devices and one-way devices are based on either nonlinear optics or magneto-optical (MO) effects. Using MO effects, unidirectional propagation can appear from a strong electromagnetic spectral asymmetry in the presence of a strong external magnetic field based on the simultaneous breaking of space and time-reversal symmetry [43]. Equally, unidirectional propagation may also occur due to the geometry of the structure [40]. Many conventional metal surfaces support localized surface plasmon polariton modes that can be excited using prism-coupling methods which, nevertheless cannot be applied in THz frequency range. Surface plasmon polaritons in the THz range are technologically important because they provide a possibility to develop subwavelength-scale device and offer the only possibility to investigate nanoscale systems in THz frequencies.

In this subsection, we focus on a magnetoplasmons performance of planar waveguides, based on highly-dispersive polaritonic InSb material, in the presence of external magnetic field, affecting the structure via the Voigt MO effect and thus imposing desired nonreciprocity (one-way propagation).

A schematic picture of the MO guiding structures of our interest and investigation is shown in Fig. 16. In fact, we have considered three configurations of InSb waveguides, namely: (1) a flat simple InSb / dielectric (air) planar boundary (see Fig. 16a)), (2) a planar InSb / air / metal (gold) planar waveguide (see Fig. 16b)), and finally a new original structure proposed, (3) a symmetric InSb / (dielectric) air / InSb planar guide (see Fig. 16c)). The purpose of an introduction of the third structure with opposite magnetizations is to increase one-way propagation region with lower or same value of the magnetic field.

Three types of guides guide consist of magnetized InSb substrate, separated from air, or gold, or InSb cover with an air guide (with the relative permittivity of air equal 1). Here, the width w and the typical length of the waveguide are $w = 15.68\,\mu$m and $300\,\mu$m, respectively. It should be noted that, within the THz frequency range, gold resembles a perfect conductor.

4.2.3 Comparison of three one-way plasmonic waveguides based on InSb

First of all, we have calculated dispersion diagrams with nonreciprocity behaviour with respect to the propagation direction for the corresponding waveguide for the magnetic

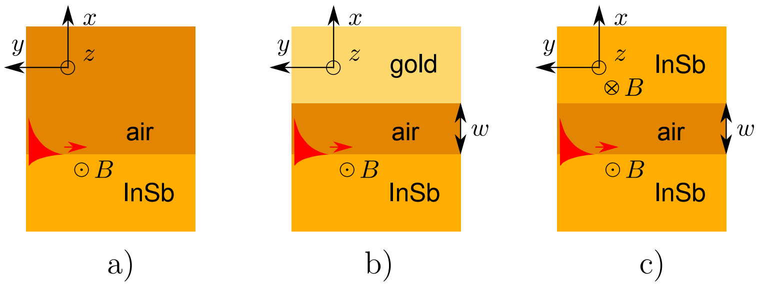

Figure 16 Schematic picture of thee one way nonreciprocal waveguides: a) simple InSb/air boundary, b) InSb/air/gold waveguide, c) InSb(+)/air/InSb(−) waveguide; (+) or (−) symbols define direction of the magnetic field.

fields $B = 0\,\mathrm{T}$ and $B = 1\,\mathrm{T}$, respectively. The results are shown in Fig. 17 where backward and forward modes create one-way propagation region. As it turned out, the one-way bandwidth of the symmetric InSb / air / InSb planar waveguide is the largest (due to opposite magnetization). In case of diagrams 17a) and 17b), we have obtained nearly perfect agreement between the MOaRCWA results and the dispersion equation [44] (however, dispersion equation [44] cannot be used to calculate the symmetric InSb / air / InSb planar waveguide). Notice that a backward propagating mode exhibits sudden frequency cut-off.

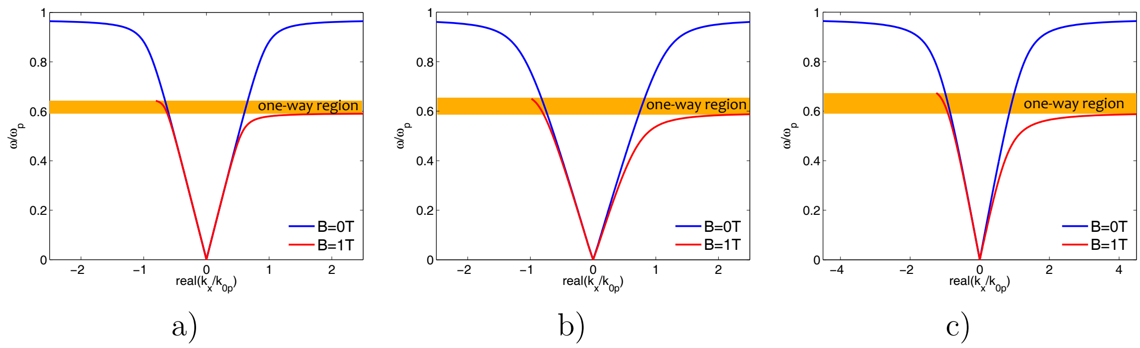

Figure 17 Dispersion diagrams for the one-way MO InSb waveguide structures of interest, for the magnetic fields applied ($B = 0$ T, $B = 1$ T, respectively): a) InSb / dielectric (air) planar boundary, b) InSb / air / metal (gold) planar waveguide, c) symmetric InSb / air / InSb planar waveguide.

Next, relative spectral transmittances T of the forward and backward propagating waves are plotted in Fig. 18, these simulations have been done with our MOaRCWA method. This nonreciprocal transmittance within the whole band gap clearly evidence potential application possibilities. Notice that the noreciprocal effect is a weak in case of simple planar boundary with the waveguide length $300\,\mu$m. Therefore, to allow the effect to increase, we have also considered the guide length of 3000 μm. As can be seen, the symmetric InSb / air / InSb planar waveguide (see in Fig. 18c)) exhibits the largest one-way propagation region.

In this section, we have analysed three configurations of nonreciprocal magnetoplasmonic waveguides formed with InSb material, applicable as one-way structures in the THz range. The analysis is based on combination of (quasi)analytical dispersion relation predictions

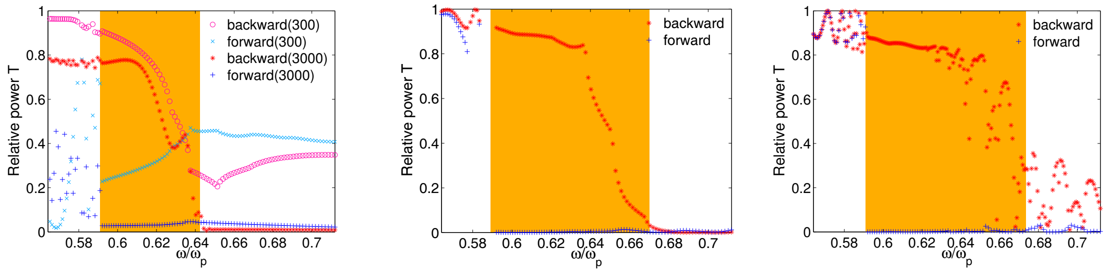

a) b) c)

Figure 18 Relative spectral transmittance T of the forward and backward propagating waves for the one-way MO InSb waveguide structures of interest: a) InSb / dielectric (air) planar boundary (two lengths of the boundary are considered: 300 μm and 3000 μm), b) InSb / air / metal (gold) planar waveguide, c) symmetric InSb / air / InSb planar waveguide.

and our magneto-optic Fourier modal method (MOaRCWA) simulations. Currently, the results of this research, in a broader context, are ready for publication.

4.3 High-Q photonic crystal nanocavities

This section summarizes the main results of an another example — the simulation of a hybrid cavity structure which was proposed within the European Action COST MP0702 as a modelling exercise [45] for a thorough comparison of the numerical techniques. The hybrid character stems from the use of different materials for cavity and waveguide. The full results of the study are published in [46]. The hybrid cavity structure, which is shown in Fig. 19, consists of a size-modulated 1D stack cavity coupled with the Si nanowire waveguide. It has been shown that such stack cavities (a simple periodic array of dielectric blocks) can reach ultrahigh quality factors (Q-factor) provided widths of the blocks (i.e. here the widths of InP sections in x direction) are properly modulated near the cavity center [47].

Structure definition
Schematic cross-section views of the structure are shown in Fig. 19. The structure consists of a cavity, coupled to an (input or output) waveguide.

The modulated cavity vein widths are

$$w(i) = w_{cav}\left[1 + \frac{(i-1)^2}{3N_{\mathrm{cav}}^2}\right],$$

with $w_{\mathrm{cav}} = 0.15\,\mu$m and $i = 1, \ldots, N_{\mathrm{cav}}$. Modulated cavity vein widths $w(i)$ are rounded to three decimal places. The following parameters remain fixed throughout all geometry: $\mathrm{InP}_y = 0.7\,\mu$m, $\mathrm{InP}_z = 0.35\,\mu$m, period $= 0.35\,\mu$m, $\mathrm{Si}_z = 0.22\,\mu$m. Some of the ladder properties are also fixed. The unmodulated “mirror” veins on each side have width (in the x-direction) $w_{mir} = 0.2\,\mu$m. After some optimizations, we used 10 mirror veins ($N_{mir} = 10$) on each side. We assume a silicon waveguide (Si, $n = 3.46$), resting on a (semi-infinite) silicon oxide layer (SiO_2, $n = 1.45$). The cavity is formed by sections of indium phosphide (InP, $n = 3.17$). On top of the oxide substrate and all around the

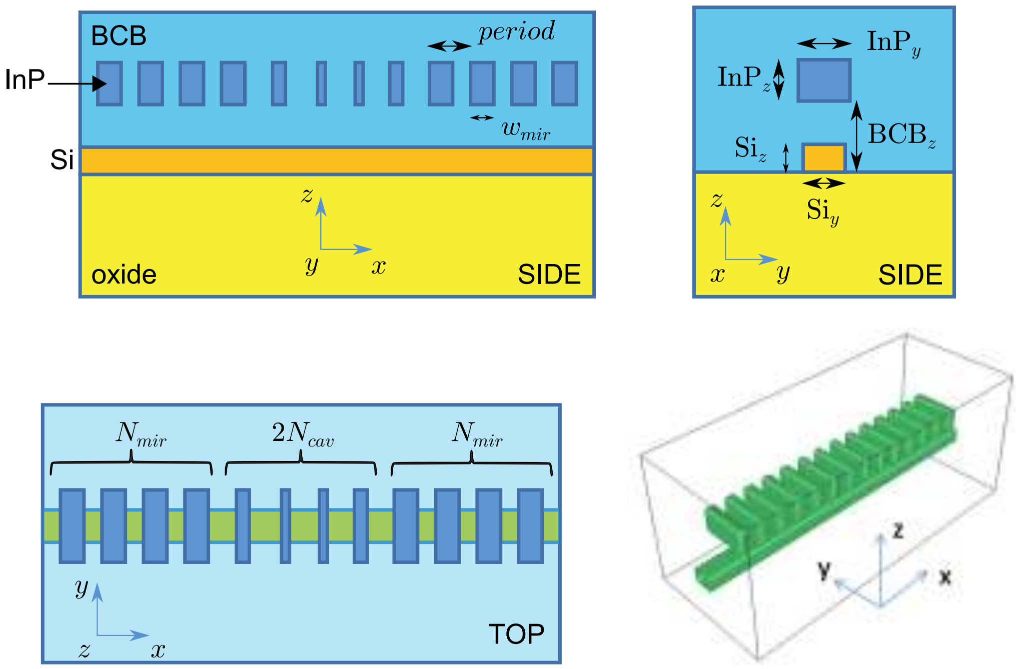

Figure 19 The PhC cavity device coupled to a waveguide. The cavity is formed by the InP sections, the waveguide functions as input/output coupler. The 3D view only shows the Si and InP sections. The structural parameters are described in the text.

cavity we considered a homogeneous material, in our case we taken the bonding material BCB (benzocyclobutene, $n = 1.54$).

The mechanism of confinement is explained as follows [47, 46]. In the center of the InP structure a Bloch mode is guided. However, when this mode propagates from the center to the side, the veins become thicker. This increase of high-index material generally means that the dispersion of the mode lowers in frequency. Eventually, at the operating frequency of the cavity, this mode becomes cut-off in the mirror sections on the side. The mode, which was propagating in the center, thus encounters a band-gap, energy can be reflected, or scattered into radiation. However, because the vein thickness change is gradual, the adjustment of the Bloch mode is very slow, leading to a substantially high probability that the forward-propagating Bloch mode is reflected into the backward-propagating mode. The latter leads to very high reflections, and, when this process happens on both sides of the center, to high-quality cavity modes. More gradual cavities will generally lead to higher quality confinement, but the mode volume will increase.

We searched for the fundamental cavity quasi-TE mode (electric field parallel with y) around wavelength $1.55\,\mu$m. Let us note that with such experimental parameters, the structure is experimentally realizable.

The main objectives of this modelling exercise were as follows:

1. study promising cavity design, determine the quality factor Q and the resonance (normalized) frequency of the fundamental cavity mode for different configurations; more detailed description of all modelling tasks is given in [45],

2. compare different simulation tools for such 3D cavity problem.

Simulation methods:

The method that were being compared are:

- Meep (FDTD) (`http://ab-initio.mit.edu/wiki/index.php/Meep`), [48] — Bjorn Maes, (University of Mons, Belgium)
- 3D finite element method (FEM) solver JCMsuite (`http://www.jcmwave.com`), [49] — Sven Burger (Zuse Institute Berlin, Germany)
- Bidirectional Eigenmode Propagation (BEP) method, [50] — Jiří Petráček, Jaroslav Luksch (Brno University of Technology, Czech Republic)
- aRCWA — Pavel Kwiecien, Ivan Richter (CTU in Prague, Czech Republic)

It should be noted that all methods simulate the device in full-vector 3D.

4.3.1 PhC cavity with waveguide

We simulated the photonic crystal cavity with a waveguide, see Fig. 19. Firstly, we simulated the dependence of the quality factor Q on the number of N_{cav}, for various constant values of the lateral Si waveguide width Si_y. An example of such simulation is shown in Fig. 20a) where Si_y is equal to $0.5\,\mu$m. Secondly, we simulated the dependence of the quality factor Q on the lateral Si waveguide width Si_y, for various constant values of N_{cav}. Here we show the result for $N_{cav} = 10$ in Fig. 20b). Graphs for different values of Si_y and $N_{cav} = 10$ are presented in [46].

As can be seen in Fig. 20, the quality factor Q is almost independent on the width of the Si_y ridge, but there is a minimum around $\mathrm{Si}_y = 0.35\,\mu$m owing to phase matching between the waveguide mode and the (central) Bloch mode in the cavity. The main discrepancies between the methods show up when strong coupling to the waveguide is involved, as this involves a delicate phase-mismatch and the need for more stringent boundary conditions. It is seen that rigorous and accurate calculation of such 3D resonant structure is still challenging.

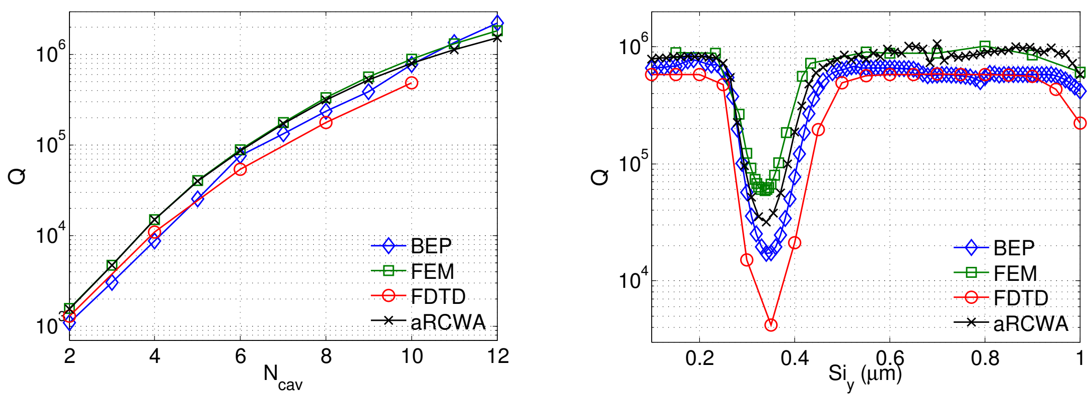

a) b)

Figure 20 Comparison of four different methods (BEP, FEM, FDTD, and aRCWA), PhC cavity with a waveguide: a) quality factor Q with respect to number of cavity sections N_{cav} ($\mathrm{Si}_y = 0.5\,\mu$m), b) quality factor Q with respect to the width of the Si_y ridge ($N_{\mathrm{cav}} = 10$).

Methods showed their good applicability. However, results differ significantly on an absolute scale. They indicate that accurate computation of 3D resonators remains a challenging problem which is further investigated.

Conclusions

This doctoral thesis statement summarizes the main selected results which were achieved during author's PhD studies. The research work was focused mainly to the topics related to the numerical simulations and theoretical analysis using periodic/aperiodic rigorous coupled wave analysis (also called Fourier modal method).

The first chapter comprised brief introduction into the modelling of photonic structures followed by the short description of the most important numerical methods in photonics today.

The second chapter was devoted to the theoretical analysis of the 3D aperiodic rigorous coupled wave analysis method which was successfully developed, tested, and applied [30]. Clearly, this 3D aRCWA method is a natural (but very difficult) generalization of the 2D case, studied previously. At first, we discussed the proper Fourier factorization technique for the 3D case including including normal vector method and its generalized modification based on complex polarization bases. After the short description of the 2D periodic RCWA method, it was shown that, with only specific modifications via absorbing layers, this method can be used efficiently for the numerical analysis of aperiodic (i.e. freely standing, isolated) photonic structures. Next, the effectiveness of the method was improved using the adaptive spatial resolution technique (the description of our proposed ASR transform is given in [11]).

In order to properly analyse full-anisotropic photonic / plasmonic structures, especially magnetooptic (Kerr effect) structures, we have developed an efficient 2D magnetooptic aperiodic rigorous coupled wave analysis technique. We applied this novel technique to several interesting cases, most importantly to the perspective MO InSb material.

The fourth chapter of the text was fully focused to showing selected examples of our computer implementation of the RCWA / aRCWA methods for three types of sub-wavelength photonic structures. Firstly, we presented an overview of our simulation results of optical sensors based on localized surface plasmon resonance for the detection of chemical and biochemical species. Secondly, we presented a specific application of the 2D Fourier-based modal magneto-optic aRCWA method capable of rigorously treating magneto-optical effects in photonic and plasmonic nanostructures. Thirdly, we presented simulation of a high-Q one-dimensional photonic crystal nanocavity

We have fulfilled all the dissertation tasks!

References

[1] P. Lalanne, J. P. Hugonin, *Perfectly matched layers as nonlinear coordinate transforms: a generalized formalization*, J. Opt. Soc. Am. A **22,** p. 1844, 2005

[2] P. Kwiecien, *Aperiodic rigorous coupled wave analysis*, master's thesis, DPE FNSPE CTU in Prague, Prague, 2008

[3] J. P. A. Bastos, N. Sadowski, *Electromagnetic modeling by finite element methods*, (Marcel Dekker, New York, 2003)

[4] K. Kawano, T. Kitoh, *Introduction to optical waveguide analysis: Solving Maxwell's equation and the Schrödinger equation*, (John Wiley & Sons, New York, 2001)

[5] K. S. Yee, *Numerical solution of initial boundary value problems involving Maxwell's equations in isotropic media*, IEEE Trans. Antennas Propagat. **14,** p. 302, 1966

[6] R. Pregla, S. Helfert, *Analysis of electromagnetic fields and waves: the method of lines*, (John Wiley & Sons, Chichester, UK, 2008)

[7] K. F. Warnick, *Numerical analysis for electromagnetic integral equations*, (Artech House, Boston, 2008)

[8] A. S. Sudbø, *Film mode matching: A versatile numerical method for vector mode field calculations in dielectric waveguides*, Pure Appl. Opt. **2,** p. 211, 1994

[9] M. G. Moharam, D. A. Pommet, E. B. Grann, T. K. Gaylord, *Stable implementation of the rigorous coupled-wave analysis for surface-relief gratings: enhanced transmittance matrix approach*, J. Opt. Soc. Am. A **12,** p. 1077, 1995

[10] E. Silberstein, P. Lalanne, J. P. Hugonin, Q. Cao, *Use of grating theories in integrated optics*, J. Opt. Soc. Am. A **18,** p. 2865, 2001

[11] J. Čtyroký, P. Kwiecien, I. Richter, *Fourier series-based bidirectional propagation algorithm with adaptive spatial resolution*, J. Lightw. Technol. **28,** p. 2969, 2010

[12] L. C. Botten, M. S. Craig, R. C. McPhedran, J. L. Adams, and J. R. Andrewartha, *The dielectric lamellar diffraction grating*, Opt. Acta **28,** p. 413, 1981

[13] P. Lalanne, G. M. Morris, *Highly improved convergence of the coupled-wave method for TM polarization*, J. Opt. Soc. Am. A **13,** p. 779, 1996

[14] G. Granet, B. Guizal, *Efficient implementation of the coupled-wave method for metallic lamellar gratings in TM polarization*, J. Opt. Soc. Am. A **13,** p. 1019, 1996

[15] L. Li, *Use of Fourier series in the analysis of discontinuous periodic structures*, J. Opt. Soc. Am. A **13,** p. 1870, 1996

[16] L. Li, *New formulation of the Fourier modal method for crossed surface-relief gratings*, J. Opt. Soc. Am. A **14,** p. 2758, 1997

[17] E. Popov, M. Neviére, *Maxwell equations in Fourier space: fast-converging formulation for diffraction by arbitrary shaped, periodic, anisotropic media*, J. Opt. Soc. Am. A **18,** p. 2886, 2001

[18] E. Popov, M. Neviére, *Grating theory: new equations in Fourier space leading to fast converging results for TM polarization*, J. Opt. Soc. Am. A **17,** p. 1773, 2000

[19] L. Li, *Note on the S-matrix propagation algorithm*, J. Opt. Soc. Am. A **20,** p. 655, 2003

[20] J. P. Bérenger, *Perfectly Matched Layer (PML) for computational electromagnetics*, (Morgan & Claypool, 2007)

[21] P. Lalanne, E. Silberstein, *Fourier-modal methods applied to waveguide computational problems*, Opt. Lett. **25,** p. 1092, 2000

[22] P. Bienstman, *Advanced boundary conditions for eigenmode expansion models*, Opt. Quantum Electron. **34,** p. 523, 2002

[23] Z. S. Sacks, D. M. Kingsland, R. Lee, J. Lee, *A perfectly matched anisotropic absorber for use as an absorbing boundary condition*, IEEE Trans. Antennas Propag. **43,** p. 1460, 1995

[24] J. Čtyroký, *Efficient boundary conditions for bidirectional propagation algorithm based on Fourier series*, J. Lightw. Technol. **27,** p. 2575, 2009

[25] J. Wu, D. M. Kingsland, R. Lee, J. Lee, *A comparison of anizotropic PML to Berenger's PML and its application to the finite element method for EM scattering*, IEEE Trans. Antennas Propag. **45,** p. 40, 1997

[26] G. Granet, *Reformulation of the lamellar grating problem through the concept of adaptive spatial resolution*, J. Opt. Soc. Am. A **16,** p. 2510, 1999

[27] T. Vallius, M. Honkanen, *Reformulation of the Fourier modal method with adaptive spatial resolution: application to multilevel profiles*, Opt. Express **10,** p. 24, 2002

[28] G. Granet, J. P. Plumey, *Parametric formulation of the Fourier modal method for crossed surface-relief gratings*, J. Opt. A: Pure Appl. Opt. **4,** p. 145, 2002

[29] P. Kwiecien, I. Richter, J. Čtyroký, *Comparison of 2D and 3D Fourier modal methods for modeling subwavelength-structured silicon waveguides*, Proc. SPIE **8306,** p. 83060Y, 2011

[30] P. Kwiecien, I. Richter, *Efficient three dimensional aperiodic rigorous coupled wave analysis technique*, Transparent Optical Networks (ICTON), 2011 13th International Conference on, p. 1, 2011

[31] P. Kwiecien, I. Richter, *Modeling of plasmonic nanostructures using efficient three dimensional aperiodic rigorous coupled wave analysis*, Frontiers in Optics 2011/Laser Science XXVII, p. JWA41, 2011

[32] L. Li, *Reformulation of the Fourier modal method for surface relief gratings made with anisotropic materials*, J. Mod. Optic. **45,** p. 1313, 1998

[33] M. H. Cho, H. Zheng, Y. Lu, Y. Lee, W. Cai, *Improved rigorous coupled-wave analysis for polar magnetic gratings*, Comput. Phys. Commun. **182,** p. 360, 2011

[34] J. Homola, *Surface plasmon resonance sensors for detection of chemical and biological species*, Chem. Rev. **108,** p. 462, 2008

[35] M. Piliarik, H. Šípová, P. Kvasnička, N. Galler, J. R. Krenn, J. Homola, *High-resolution biosensor based on localized surface plasmons*, Opt. Express **20,** p. 672, 2012

[36] B. Špačková, P. Lebrušková, H. Šípová, P. Kwiecien, I. Richter, J. Homola, *Ambiguous Refractive Index Sensitivity of Fano Resonance on an Array of Gold Nanoparticles*, Plasmonics **9,** p. 729, 2014

[37] U. Fano, *Effects of configuration interaction on intensities and phase shifts*, Phys. Rev. **124,** p. 1866, 1961

[38] D. Bedeaux, J. Vlieger, *Optical Properties of Surfaces*, (Imperial College Press, 2002)

[39] V. I. Belotelov, I. A. Akimov, M. Pohl, V. A. Kotov, S. Kasture, A. S. Vengurlekar, Achanta Venu Gopal, D. R. Yakovlev, A. K. Zvezdin, M. Bayer, *Enhanced magneto-optical effects in magnetoplasmonic crystals*, Nat. Nano. **6,** p. 370, 2011

[40] V. Kuzmiak, A. A. Maradudin, *Asymmetric transmission of surface plasmon polaritons*, Phys. Rev. A **86,** p. 155117, 2012

[41] A. Boardman, N. King, Y. Rapoport, L. Velasco, *Gyrotropic impact upon negatively refracting surfaces*, New J. Phys. **7,** p. 191, 2013

[42] B. Hu, Q. J. Wang, Y. Zhang, *Broadly tunable one-way terahertz plasmonic waveguide based on nonreciprocal surface magneto plasmons*, Opt. Lett. **37,** p. 1895, 2012

[43] A. Figotin, I. Vitebsky, *Nonreciprocal magnetic photonic crystals*, Phys. Rev. E **63,** p. 066609, 2001

[44] V. A. Dmitriev, A. O. Silva, *Nonreciprocal properties of surface plasmon-polaritons at the interface between two magnetized media: exact analytical solutions*, PIER Lett. **21,** p. 177, 2011

[45] B. Maes, F. Raineri, T. Karle, *Hybrid photonic crystal cavity modelling exercise*, (COST MP0702, cost-mp0702.nit.eu/cost-mp0702/working-group-2K, 2010)

[46] B. Maes, J. Petráček, S. Burger, P. Kwiecien, J. Luksch, I. Richter, *Simulations of high-Q optical nanocavities with a gradual 1D bandgap*, Opt. Express **21,** p. 6794, 2013

[47] M. Notomi and E. Kuramochi and H. Taniyama, *Ultrahigh-Q Nanocavity with 1D Photonic Gap*, Opt. Express **16,** p. 11095, 2008

[48] A. F. Oskooi, D. Roundy, M. Ibanescu, P. Bermel, J.D. Joannopoulos, S. G. Johnson, *Meep: A flexible free-software package for electromagnetic simulations by the FDTD method*, Computer Physics Communications **181,** p. 687, 2010

[49] J. Pomplun, S. Burger, L. Zschiedrich, F. Schmidt, *Adaptive finite element method for simulation of optical nano structures*, physica status solidi (b) **244,** p. 3419, 2007

[50] G. Sztefka, H.-P. Nolting, *Bidirectional eigenmode propagation for large refractive index steps*, IEEE Photon. Technol. Lett. **5,** p. 554, 1993

Author’s selected publications

- **Journal Articles**

B. Špačková, P. Lebrušková, H. Šípová, **P. Kwiecien**, I. Richter, J. Homola, *Ambiguous refractive index sensitivity of Fano resonance on an array of gold nanoparticles*, Plasmonics **9**, p. 729, 2014

J. Čtyroký, **P. Kwiecien**, I. Richter, *Analysis of hybrid dielectric-plasmonic slot waveguide structures with 3D Fourier Modal Methods*, J. Eur. Opt. Soc, Rapid Publ. 8, 2013

B. Maes, J. Petráček, S. Burger, **P. Kwiecien**, J. Luksch, I. Richter, *Simulations of high-Q optical nanocavities with a gradual 1D bandgap*, Opt. Express **21**, p. 6794, 2013

J. Čtyroký, **P. Kwiecien**, I. Richter, *Fourier series-based bidirectional propagation algorithm with adaptive spatial resolution*, J. Lightwave Technol. **28**, p. 2969, 2010

- **Conference Proceedings**

I. Richter, **P. Kwiecien**, J. Fiala, J. Petráček, Y. Ekşioğlu, V. Kuzmiak, J. Čtyroký, *Physics and advanced simulations of photonic and plasmonic structures*, Transparent Optical Networks (ICTON), 2014 16th International Conference on, 2014

P. Kwiecien, J. Fiala, L. Štolcová, J. Proška, I. Richter, *Approaches to electromagnetic simulations of advanced SERS substrates*, Proc. Nanocon 2014, 2014

J. Fiala, **P. Kwiecien**, I. Richter, *Studies on Fano resonances in subwavelength plasmonic nanostructures*, PIERS Proc. **2013**, p. 439, 2013

P. Kwiecien, V. Kuzmiak, I. Richter, and J. Čtyroký, *Properties of one-way magnetooptic nanostructures in THz range*, PIERS Proc. **2013**, p. 730, 2013

J. Čtyroký, **P. Kwiecien**, I. Richter, *Dispersion properties of subwavelength frating SOI waveguides*, PIERS Proc. **2013**, p. 1613, 2013

I. Richter, **P. Kwiecien**, J. Čtyroký, *Advanced photonic and plasmonic waveguide nanostructures analyzed with Fourier modal methods*, Transparent Optical Networks (ICTON), 2013 15th International Conference on, 2013

B. Špačková, N.S. Lynn, J. Homola, **P. Kwiecien**, I. Richter, *Consideration of photonic and mass-transfer aspects on the performance of a biosensor based on localized surface plasmons on an array of gold cylinders*, Sensors, 2012 IEEE p. 1, 2012

J. Čtyroký, **P. Kwiecien**, I. Richter, P. Cheben, *Analysis of couplers between photonic nanowires and subwavelength grating waveguides*, Proc. SPIE **8781**, p. 87810B, 2012

J. Fiala, **P. Kwiecien**, I. Richter, *The physics and design possibilities of plasmonic-based fishnet metamaterial structures*, Proc. SPIE **8697**, p. 86971X, 2012

P. Kwiecien, I. Richter, J. Čtyroký, *Novel types of dielectric loaded surface plasmon polariton waveguides and structures*, Proc. SPIE **8697**, p. 86971Y, 2012

J. Čtyroký, **P. Kwiecien**, I. Richter, J. Petráček, J. Luksch, *Modal methods for 3D modelling of advanced photonic structures*, Transparent Optical Networks (ICTON), 2012 14th International Conference on, 2012

J. Petráček, B. Maes, S. Burger, J. Luksch, **P. Kwiecien**, I. Richter, *Simulation of high-Q nanocavities with 1D photonic gap*, Transparent Optical Networks (ICTON), 2012 14th International Conference on, 2012

J. Petráček, J. Luksch, B. Maes, S. Burger, **P. Kwiecien**, I. Richter, *Simulation of photonic crystal nanocavities using a bidirectional eigenmode propagation algorithm: a comparative study*, Proc. MINAP 2012, p. 109, 2012

P. Kwiecien, I. Richter, J. Čtyroký, *Application of Fourier modal methods to simulating novel plasmonic guiding nanostructures*, AIP Conf. Proc. **1475**, p. 71, 2012

P. Kwiecien, I. Richter, J. Čtyroký, *Comparison of 2D and 3D Fourier modal methods for modeling subwavelength-structured silicon waveguides*, Proc. SPIE **8306**, p. 83060Y, 2011

P. Kwiecien, I. Richter, *Efficient three dimensional aperiodic rigorous coupled wave analysis technique*, Transparent Optical Networks (ICTON), 2011 13th International Conference on, 2011

P. Kwiecien, I. Richter, *Modeling of plasmonic nanostructures using efficient three dimensional aperiodic rigorous coupled wave analysis*, Frontiers in Optics 2011/Laser Science XXVII, p. JWA41, 2011

J. Fiala, **P. Kwiecien**, M. Šiňor, I. Richter, *Analysis of subwavelength-patterned plasmonic structures with approximate models*, Frontiers in Optics 2011/Laser Science XXVII, p. JWA37, 2011

P. Kwiecien, I. Richter, P. Bienstman, *Improvements of Aperiodic Rigorous Coupled Wave Analysis*, Frontiers in Optics 2009/Laser Science XXV/Fall 2009 OSA Optics & Photonics Technical Digest, p. FTuO7, 2009

J. Fiala, **P. Kwiecien**, I. Richter, *Theory and simulations of enhanced transmission through plasmonic sub-wavelength structures*, Frontiers in Optics 2009/Laser Science XXV/Fall 2009 OSA Optics & Photonics Technical Digest, p. FWC7, 2009